

# Nanoscale magnetometry of a synthetic three-dimensional spin texture

Ricardo Javier Peña Román,<sup>\*,†,‡,¶</sup> Sandip Maity,<sup>†,‡</sup> Fabian Samad,<sup>§,||</sup> Dinesh Pinto,<sup>†,⊥</sup> Simon Josephy,<sup>#</sup> Andrea Morales,<sup>#</sup> Attila Kákay,<sup>§</sup> Klaus Kern,<sup>†,⊥</sup> Olav Hellwig,<sup>§,||</sup> and Aparajita Singha<sup>\*,†,‡,¶</sup>

<sup>†</sup>*Max Planck Institute for Solid State Research, 70569 Stuttgart, Germany*

<sup>‡</sup>*Institute of Solid State and Materials Physics, Dresden University of Technology, 01069 Dresden, Germany*

<sup>¶</sup>*Würzburg-Dresden Cluster of Excellence ct.qmat, 01069 Dresden, Germany*

<sup>§</sup>*Institute of Ion Beam Physics and Materials Research, Helmholtz-Zentrum Dresden-Rossendorf, 01328 Dresden, Germany*

<sup>||</sup>*Institute of Physics, Chemnitz University of Technology, 09107 Chemnitz, Germany*

<sup>⊥</sup>*Institute de Physique, École Polytechnique Fédérale de Lausanne, CH-1015 Lausanne, Switzerland*

<sup>#</sup>*QZabre AG, 8050 Zurich, Switzerland*

E-mail: [ricardo.pena\\_roman@tu-dresden.de](mailto:ricardo.pena_roman@tu-dresden.de); [aparajita.singha@tu-dresden.de](mailto:aparajita.singha@tu-dresden.de)

## Abstract

Multilayered synthetic antiferromagnets (SAFs) are artificial three-dimensional (3D) architectures engineered to create novel, complex, and stable spin textures. Non-invasive and quantitative nanoscale magnetic imaging of the two-dimensional stray field profile at the sample surface is essential for understanding the fundamental properties of the spin-structure and being able to tailor them to achieve new function-

alities. However, the deterministic detection of spin textures and their quantitative characterization on the nanoscale remain challenging. Here, we use nitrogen-vacancy scanning probe microscopy (NV-SPM) under ambient conditions to perform the first quantitative vector-field magnetometry measurements in the multilayered SAF  $[(\text{Co}/\text{Pt})_5/\text{Co}/\text{Ru}]_3/(\text{Co}/\text{Pt})_6$ . We investigate nanoscale static and dynamic properties of antiferromagnetic domains with boundaries hosting "one-dimensional" ferromagnetic stripes with  $\sim 100$  nm of width and periodic modulation of the magnetization. By employing NV-SPM measurements in different imaging modes and involving NV-probes with various crystallographic orientations, we demonstrated distinct fingerprints emerging from GHz-range spin noise and constant stray fields on the order of several mT. This provides quantitative insights into the structure of domains and domain walls, as well as, into magnetic noise associated with thermal spin-waves. Our work opens up new opportunities for quantitative vector-field magnetometry of modern magnetic materials with tailored 3D spin textures and stray field profiles, and potentially novel spin-wave dispersions—in a quantitative and non-invasive manner, with exceptional magnetic sensitivity and nanometer scale spatial resolution.

## Keywords

Synthetic antiferromagnet, Multilayered structures, 3D spin texture, Domain wall, NV-magnetometry,  $T_1$  relaxometry, Magnetic noise.

## Introduction

Synthetic antiferromagnets (SAFs) are artificial magnetic systems that offer unique opportunities for fundamental research and applications due to their highly tunable static and dynamic properties.<sup>1–5</sup> In particular, SAFs present stable magnetic textures and high-frequency spin dynamics, which are ideal properties for magnetic storage technologies and spintronic devices.<sup>6–10</sup> Multilayered SAFs are systems with a more complex layered structure, designed

to tune magnetic energy terms to create novel magnetic textures.<sup>2,11–14</sup> For instance, systems with perpendicular magnetic anisotropy (PMA) can be engineered to stabilize stripe and bubble domain states,<sup>15</sup> to induce a domain wall (DW) transition from antiferromagnetic (AF) DWs to DWs with ferromagnetic (FM) cores,<sup>16</sup> or to stabilize FM domains separated by AF DWs when the interlayer exchange energy is reduced below the demagnetization energy<sup>17</sup>. From the dynamic point of view, dipolar interaction can affect the spin-wave modes and induce nonreciprocity on the spin-wave dispersion<sup>18,19</sup>, giving rise to complex spin-wave propagation. Additionally, multilayered structures with periodic magnetic stripe domain patterns exhibit spin-wave modes and dispersion relations analogous to those of a one-dimensional magnonic crystal, which can be used to control spin-wave propagation.<sup>20,21</sup> Therefore, these types of multilayered architectures are a powerful and application friendly approach to develop new magnetic materials with spin textures and properties useful to improve the performance of SAFs and to design the next generation of magnetic devices.<sup>22–25</sup>

The direct imaging of the two-dimensional stray magnetic field profile at the sample surface with nanoscale spatial resolution can provide insights into the properties of individual domains and DWs, which is a crucial step toward understanding and improving the fundamental properties and performance of multilayered SAFs. Magnetic force microscopy (MFM) combined with macroscopic magnetometry have been employed to investigate multilayered SAFs and to connect the nanoscale magnetism of every domain/DW with the macroscopically observed properties, such as magnetization or magnetic hysteresis.<sup>11–13,16,17,26–28</sup> However, the field of a few tens of mT of the MFM probe<sup>29</sup> can induce reversible changes or irreversible re-orientation of the magnetic moments while scanning the sample,<sup>30–32</sup> hindering access to the intrinsic undisturbed magnetic texture. Furthermore, macroscopic magnetometry provides only information about the average behavior of a large number of magnetic domains. Moreover, many magnetic imaging techniques probe only static properties non-quantitatively and lack the sensitivity required to investigate phenomena with weak stray magnetic field (such as AF order). Therefore, despite the enormous effort in the last few years, there is still a re-

maining challenge regarding the deterministic detection of magnetic textures in multilayered SAFs, along with the local, quantitative, and non-invasive characterization of both static and dynamic properties.

Nitrogen-Vacancy scanning probe microscopy (NV-SPM) has recently gained immense interest as a robust quantum sensing tool. It utilizes the quantum properties of a single NV defect in diamond for quantitative and non-invasive magnetic imaging, where the magnetic vector-field sensitivity can be as high as nT with an exceptional nanoscale spatial resolution, in the range of tens of nanometers.<sup>33-38</sup> NV-SPM has been previously employed to investigate ultra-thin SAFs or FM thin films to determine the nature of DWs and strength of the Dzyaloshinskii-Moriya interaction,<sup>39-41</sup> DW motion,<sup>42,43</sup> spin-wave dispersion and magnetic noise.<sup>44,45</sup> In such systems, the magnetic thickness is typically less than 2 nm with a few mT of stray field, for which unwanted effects that often make quantitative measurements difficult, such as spin-mixing of the NV-spin states and suppression of the quantum sensor's signal due to high off-axis stray fields, are not present. Consequently, magnetic imaging of thick multilayered SAFs with complex and novel spin textures and dynamics, producing both a large stray field of tens of mT and spin noise, remained unexplored using NV-SPM.

In this work, we use NV-SPM under ambient conditions to investigate the magnetic texture of the multilayered SAF of the type  $[(\text{Co/Pt})_{X-1}/\text{Co/Ru}]_{N-1}/(\text{Co/Pt})_X$  with  $X = 6$ , and  $N = 4$ . We explore the domains and DWs structure, as well as their static and dynamic properties, by performing measurements in different imaging modes and employing NV-probes with various crystallographic orientations to identify distinctive fingerprints arising from both constant stray magnetic fields and spin noise. We use optically detected magnetic resonance (ODMR) and  $T_1$  relaxometry measurements to demonstrate the presence of both sample stray fields on the order of mT and spin noise in the GHz range. We perform qualitative magnetic imaging with commercial diamond probes containing a single NV and fabricated from (100)- and (110)-oriented diamond crystals.<sup>46</sup> By using a (111)-oriented single NV probe,<sup>47</sup> we quantitatively resolve the nanoscale DW structure and the spatial

distribution of the sample stray field. Combining this with micromagnetic simulation, we confirm a three-dimensional (3D) model of the spin texture that agrees well with our quantitative measurements. Our work opens novel opportunities to understand and characterize static and dynamic properties in layered architectures with complex magnetic textures and spin-waves, quantitatively and non-invasively, with exceptionally high magnetic sensitivity and nanometer-scale spatial resolution.

## Results and discussions

### NV-SPM imaging in a multilayered SAF

As illustrated in Figure 1(a), NV-SPM employs a single NV defect in a diamond scanning probe (see section 1 in supplementary information (SI)). The NV sensor is used to map the sample surface and spatially resolve the magnetic texture. Due to its spin-dependent photoluminescence (PL), the NV-spin state can be optically initialized with a green laser (515 nm) and read out by detecting the red NV-PL signal in the wavelength range of 650-850 nm (see methods). Qualitative magnetic imaging can be performed by mapping the intensity of the NV-PL signal while scanning the sample. For direct quantification of the sample stray field by ODMR, microwave (MW) excitation is applied to promote the NV spin transition. Thereby, the stray magnetic field from the sample is determined from the Zeeman splitting produced by its component along the NV-axis, which is oriented along the  $\langle 111 \rangle$  crystallographic direction in the diamond probe. The orientation of the NV-axis is defined by the angles  $(\theta_{\text{NV}}, \varphi_{\text{NV}})$  in the laboratory frame. From our ODMR measurements under ambient conditions, we estimate a DC magnetic field sensitivity of  $\sim 2 \mu\text{T}/\sqrt{\text{Hz}}$ . The value of the detected stray field and the spatial resolution for magnetic imaging depend on the NV-sample distance, which is  $d_{\text{NV}} = 36\text{-}76 \text{ nm}$  for all our measurements (see Section 2 in SI).

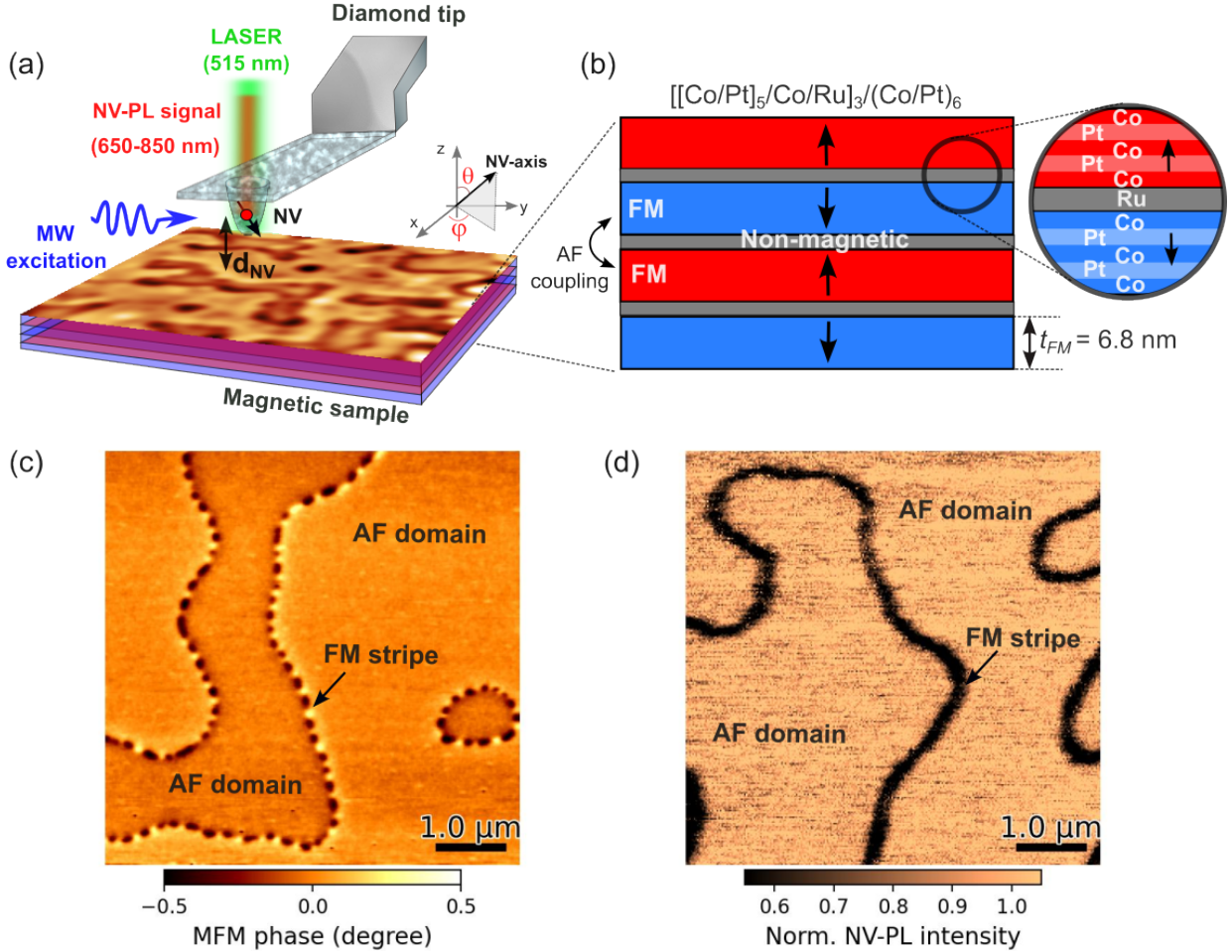


Figure 1: **Magnetic imaging of a multilayered synthetic antiferromagnet.** (a) A single NV center in a scanning diamond probe is used for sensing the magnetic field and noise of the sample at a given NV-sample distance  $d_{NV}$ . The NV spin state is optically initialized with a green laser (515 nm) and read out by detecting the NV-PL signal (650-850 nm) after interaction with the sample. Qualitative magnetic imaging is possible via MW-free NV-PL maps with and without applying external magnetic field. For ODMR measurements, MW excitation in the GHz range is required to promote the electron spin transition. The sample stray field and noise are sensed along and perpendicular to the NV-axis, respectively. The angles ( $\theta_{NV}, \varphi_{NV}$ ) define the orientation of the NV-axis in the laboratory frame. (b) Schematic structure of the multilayered SAF  $[[Co(0.55\text{ nm})/Pt(0.70\text{ nm})]_5/Co(0.55\text{ nm})/Ru(0.75\text{ nm})]_3/[Co(0.55\text{ nm})/Pt(0.70\text{ nm})]_6$ . (c)  $6\text{ }\mu\text{m} \times 6\text{ }\mu\text{m}$  MFM image of the multilayered SAF. (d)  $6\text{ }\mu\text{m} \times 6\text{ }\mu\text{m}$  NV-PL quenching map recorded with a (100)-oriented NV probe and without applying external magnetic field, pixel size 24 nm/px and acquisition time 24 ms/px. The intensity is normalized with respect to the average counts on the AF domains (bright areas).

Figure 1(b) illustrates the structure of the multilayered SAF investigated in this work.

The stacking of 6 Co layers with 5 Pt interlayers give rise to FM building blocks with PMA. i.e. out-of-plane (OOP) magnetization parallel or antiparallel to the film normal axis. The insertion of a non-magnetic material like Ru introduces an AF-coupling between adjacent FM blocks through the Ruderman–Kittel–Kasuya–Yosida exchange interaction. The strength of the AF-exchange interaction can be tuned via the Ru thickness.<sup>1,2,12</sup> In our sample, we have the AF-coupling of four FM blocks, and the full structure is described as  $[[\text{Co}(0.55 \text{ nm})/\text{Pt}(0.70 \text{ nm})]_5/\text{Co}(0.55 \text{ nm})/\text{Ru}(0.75 \text{ nm})]_3/[\text{Co}(0.55 \text{ nm})/\text{Pt}(0.70 \text{ nm})]_6$ . The numbers in nm correspond to the thickness of every thin film along the stacking. Thus the magnetic thickness of a single FM block is  $t_{FM} = 5 \times [0.55 \text{ nm}(\text{Co}) + 0.70 \text{ nm}(\text{Pt})] + 0.55 \text{ nm}(\text{Co}) = 6.8 \text{ nm}$ . The hysteresis curve measured on this sample shows four discrete steps (see section 3 in SI), where every step corresponds to the magnetic reversal of one of the four FM blocks, with an average saturation magnetization  $M_s = (833 \pm 83) \text{ kA/m}$  for configurations with a full magnetization pointing up/down.

MFM images recorded after sample saturation with an in-plane applied field reveal a remanent state constituted by one-dimensional FM stripe domains with periodic bright and dark contrast at the boundary between AF domains<sup>12,16</sup>, as shown in Figure 1(c). The AF domain sizes are primarily in the micrometer range, with  $\sim 100 \text{ nm}$ -wide FM stripes and average periodicity of the contrast of  $\sim 300 \text{ nm}$  (see section 3 in SI). The width of the stripes and the periodicity of the contrast can vary slightly from one stripe to another, but typically remain on the order of hundreds of nanometers. The alternating bright and dark contrast observed along the FM stripe, as well as, the slight difference in magnetic contrast between adjacent AF domains, originates from the parallel and antiparallel alignment of the sample stray field and the magnetic MFM tip. Such magnetic texture has been observed by Hellwig *et al.* in similar samples with various  $X$ ,  $N$ , and layer thicknesses.<sup>12,16</sup> However, gaining further quantitative microscopic details on the spin texture of domains and DWs along with their dynamic properties are beyond the scope of standard MFM measurements.

To this end, we employ the NV-SPM approach. Figure 1(d) shows an image acquired in

the NV-PL quenching mode with a (100)-oriented NV probe. The NV-PL signal is detected pixel by pixel as the sample is scanned across the NV tip which is kept stationary at the focus of the initializing green laser beam. MW excitation is not applied during the measurements in this imaging mode. We observe large bright areas on the AF domains. Along the FM stripe domains the PL signal is quenched by about 40%. The NV-PL signal can be quenched either due to spin-mixing effects induced by strong off-axis stray fields<sup>48</sup> or due to a decrease of the spin-relaxation time ( $T_1$ ) in case spin noise is present with frequencies resonant with the NV spin transition.<sup>44,49</sup> Contrary to MFM measurements, there is no periodic variation of the contrast. However, MFM-like contrast can be achieved in NV-PL maps only after applying a suitable off-axis (not aligned with the NV-axis) external magnetic field, as described in the following section.

## MFM-like contrast in NV-PL quenching maps

We determined  $(\theta_{\text{NV}}, \varphi_{\text{NV}}) = (113^\circ, 270^\circ)$  for the (100)-oriented NV probe (see section 2 in SI). Figure 2(a) illustrates the relative orientation between the single NV-spin and the magnetization of the sample. We observe different contrast between the AF domains and along the FM stripes, when an off-axis external field is applied during the acquisition of NV-PL images, as can be seen in Figure 2(b) for  $B_{\text{ext}} = 20$  mT. The external field is applied along  $(\theta_{\text{ext}}, \varphi_{\text{ext}}) = (54.8^\circ, 180^\circ)$ , with an angle  $\alpha \approx 103^\circ$  with respect to the NV-axis. The image is similar to the one obtained with MFM, but without the inherent local effect of the field from the tip; here, the external field is globally and uniformly applied to both sample and tip. High-resolution images of a FM stripe between AF domains are shown in Figure 2(c). The contrast is modified in the NV-PL quenching images when the intensity of the applied field is increased from 0 mT to 60 mT due to field compensation or competition between the external and sample stray field.

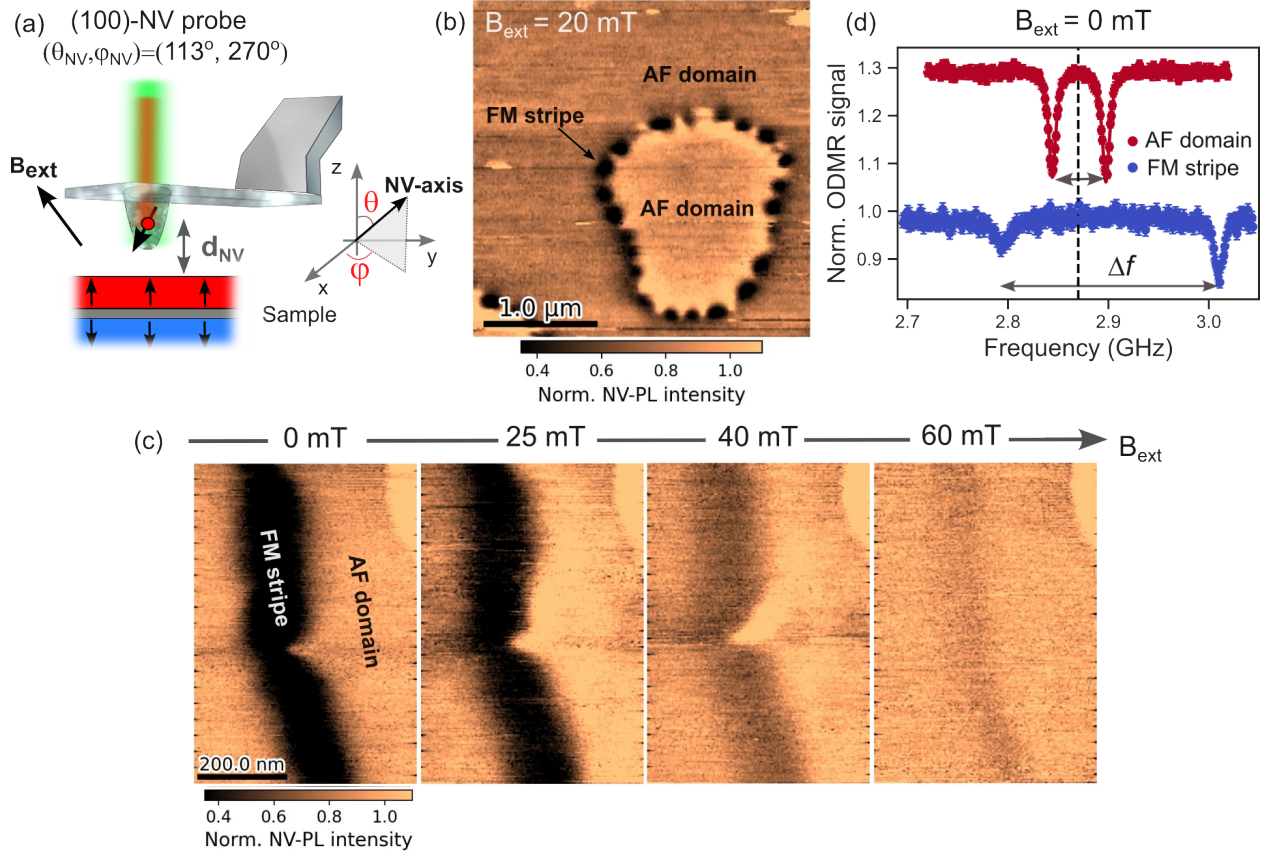


**Figure 2: Effects of an external off-axis magnetic field on the contrast of NV-PL maps.** (a) Schematic illustration of the relative orientation between the (100)-oriented NV probe and the sample magnetization during NV-SPM measurements. The direction of the NV-axis is determined by the coordinates  $(\theta_{NV}, \varphi_{NV}) = (113^\circ, 270^\circ)$  in the laboratory frame. (b)  $3 \mu\text{m} \times 3 \mu\text{m}$  NV-PL quenching map recorded in presence of an external off-axis field  $B_{ext} = 20$  mT applied along  $(\theta_{ext}, \varphi_{ext}) = (54.8^\circ, 180^\circ)$ . Pixel size 100 nm/px and acquisition time 25 ms/px. (c) High resolution NV-PL quenching maps ( $500 \text{ nm} \times 720 \text{ nm}$ ) on a FM DW recorded at different value for the external field. Pixel size 4 nm/px and acquisition time 25 ms/px. (d) Normalized and vertically shifted ODMR spectra measured on the AF domain and FM DW without external field.

To understand the origin of the NV-PL quenching and explain the effect of the external field on the contrast of the NV-PL maps, we first performed local ODMR measurements without any external field. Figure 2(d) shows ODMR spectra measured locally when the tip is on an AF domain and on a FM stripe domain (see section 4 in SI for additional measurements). On the AF domain, we observe an ODMR spectrum with around 20 % of contrast, and the splitting  $\Delta f$  is symmetric with respect to the zero-field splitting (ZFS)

frequency  $f_0 = 2.87$  GHz indicated by the vertical dashed line. However, in contrast, the splitting  $\Delta f$  is asymmetric with respect to  $f_0$  on the FM stripe and the contrast also decreases to less than 10% for the dip at 2.80 GHz. The features observed on the FM stripe are indications that the NV-PL quenching is a consequence of spin-mixing effects<sup>48</sup> produced by components of several mT of the sample stray magnetic field that are perpendicular to the NV-axis. At some locations along the FM stripe, the stray field can be too strong to perform any ODMR measurements (see section 4 in SI). When spin-mixing effects are present, the NV-PL intensity is reduced since there are NV-spin transitions involving states that are linear combinations of dark ( $m_s = \pm 1$ ) and bright ( $m_s = 0$ ) states. NV-PL quenching is expected along the boundary between AF domains as these are the regions in the sample where we have FM order with a strong field.

To further explain the effect of the external off-axis field and the MFM-like contrast in NV-SPM, we use the model proposed in Section 5 of the SI. We consider all the field components perpendicular to the NV-axis that could produce quenching of the PL signal due to spin-mixing. The net magnetic field perpendicular to the NV-axis has contributions from the external off-axis field ( $\mathbf{B}_{\text{ext}}$ ) and the sample stray magnetic field ( $\mathbf{B}_s$ ):

$$\mathbf{B}_{\text{total}}^{(\perp, \text{NV})} = \mathbf{B}_{\text{ext}}^{(\perp, \text{NV})} + \mathbf{B}_s^{(\perp, \text{NV})}, \quad (1)$$

where :

$$B_i^{(\perp, \text{NV})} = B_i \sqrt{1 - [\sin \theta_i \sin \theta_{\text{NV}} \cos(\varphi_i - \varphi_{\text{NV}}) + \cos \theta_i \cos \theta_{\text{NV}}]^2}. \quad (2)$$

with  $i = \text{ext}$ , or  $s$ . To simplify the description, we consider only the components of the stray field of the sample that are parallel and antiparallel to the sample surface. That is, components with  $(\theta_s, \varphi_s) = (0^\circ, 0^\circ)$  and  $(\theta_s, \varphi_s) = (180^\circ, 0^\circ)$ , for OOP magnetization pointing up and down, respectively. The angle between these OOP stray field components and the NV-axis are  $113^\circ$  and  $67^\circ$ , respectively. Due to the magnetic field compensation, different degrees of quenching are expected for regions where  $B_{\text{ext}}^{(\perp, \text{NV})}$  and  $B_s^{(\perp, \text{NV})}$  are parallel

or antiparallel. For example, considering the values  $B_s = \pm 5$  mT for the stray field on the FM stripe (which is enough to produce spin-mixing in the case of a large-angle off-axis field<sup>48</sup>) and  $B_{\text{ext}} = 20$  mT, from equation (1) and (2) we can obtain  $B_{\text{total}\uparrow}^{(\perp,\text{NV})} = 24$  mT and  $B_{\text{total}\downarrow}^{(\perp,\text{NV})} = 15$  mT for regions where the sample stray field components are pointing up and down, respectively. We assume that the relative degree of quenching produced by these two fields in the NV-PL signal is proportional to the difference normalized by the total field. i.e.  $|B_{\text{total}\uparrow}^{(\perp,\text{NV})} - B_{\text{total}\downarrow}^{(\perp,\text{NV})}|/[B_{\text{total}\uparrow}^{(\perp,\text{NV})} + B_{\text{total}\downarrow}^{(\perp,\text{NV})}] = 0.23$ . We interpret this as a relative contrast of  $C = 23\%$  between the dark and the bright areas in the NV-PL maps, leading to the MFM-like contrast in Figure 2(b). This relative contrast decreases when increasing the intensity of the external field (see section 5 in SI), being  $C = 7\%$  for  $B_{\text{ext}} = 60$  mT. This explains the almost vanishing contrast on the FM stripe in Figure 2(c). It is noteworthy that the effect is reversible. Once the external field is switched off, a PL map similar to that for  $B_{\text{ext}} = 0$  mT is recovered. For  $B_{\text{ext}} = 0$  mT, the contribution is from the sample, i.e.,  $B_s = \pm 5$  mT, which produces the same degree of quenching. In general,  $B_s$  is not fully  $\pm 5$  mT; it can be smaller or larger. However, for spin-mixing, the difference in the PL drop produced by a variation in  $B_s$  of 1-5 mT would be around 5%.<sup>48,50</sup> Thus, it would not be possible to differentiate between the PL quenching produced by two close values of the stray field with a significant contrast. Therefore, the contrast along the FM stripe and within the AF domains will be uniform for domains with magnetization pointing upward and downward, in the absence of an off-axis  $B_{\text{ext}}$ , as also observed in Figure 1(d). Additional NV-PL maps with MFM-like contrast in a different sample are shown in section 6 of the SI.

## Internal structure of the ferromagnetic stripe

To avoid having strong stray field components producing spin-mixing and be able to perform quantitative measurements, we employed a (111)-oriented NV probe. With this diamond probe we determined  $(\theta_{\text{NV}}, \varphi_{\text{NV}}) = (180^\circ, 0^\circ)$  (see section 2 in SI). Therefore, we can assume a collinear alignment between the NV-axis and the sample magnetization, as illustrated in

Figure 3(a). An NV-PL quenching map recorded without applying an external field is shown in Figure 3(b). The PL signal is quenched only along the FM stripe between AF domains. However, in contrast to the case of (100)-NV tip, the local ODMR measurements in Figure 3(c) show symmetric Zeeman splitting  $\Delta f$  with respect to  $f_0$ , on both the AF domain and the FM stripe (see Section 7 in SI for additional measurements). Based on these ODMR results, we can rule out a PL-quenching induce by spin-mixing. Thus, we attribute the NV-PL quenching to magnetic noise.<sup>44</sup> From the spectra depicted in Figure 3(c), we can determine a magnetic field projected on the NV-axis of 0.6 mT and 4.0 mT on both the AF domain and the FM stripe, respectively.

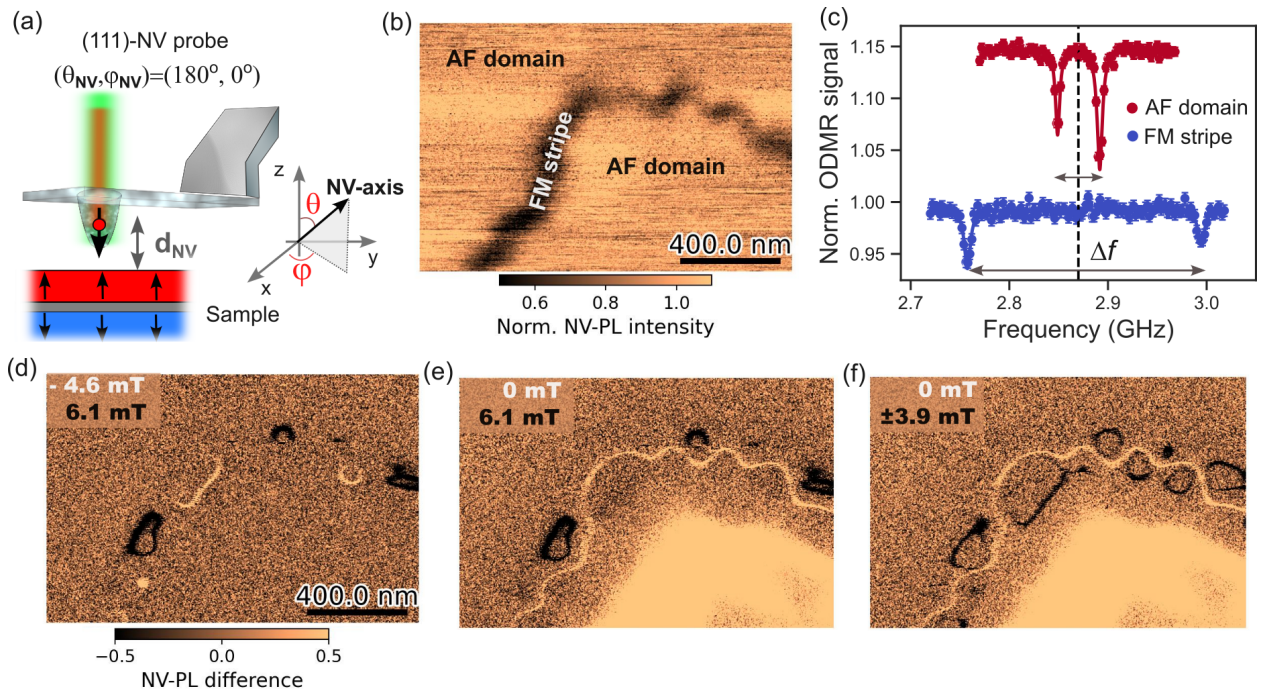


Figure 3: **Resolving the internal structure of the FM stripe.** (a) Schematic illustration of the relative orientation between the NV-axis of the (111)-oriented NV probe and sample magnetization during NV-SPM measurements. The direction of the NV-axis is determined by the coordinates  $(\theta_{NV}, \varphi_{NV}) = (180^\circ, 0^\circ)$  in the laboratory frame. (b) NV-PL quenching map recorded without external field. (c) Normalized and vertically shifted ODMR spectra measured on the AF domain and FM DW. (d)-(f) Dual Iso-B contour images. The size, pixel size and acquisition time for all the images shown in this figure are  $1.5 \mu\text{m} \times 1.0 \mu\text{m}$ , 4 nm/px and 20 ms/px, respectively.

To gain quantitative insight into the FM texture of the stripes observed between the AF domains in NV-PL quenching maps and MFM images, we first performed NV-SPM measurements in the iso-B imaging mode by acquiring NV-PL maps with a given MW frequency to resolve iso-magnetic field contours<sup>50</sup> (see section 8 in SI). Dual iso-B images are obtained by subtracting the PL images at two fixed frequencies. In this case, we observe contour maps with two different values of the sample stray field. The dual iso-B image in Figure 3(d) reveals contours of FM domains in the nanometer range with a stray field  $B_{\text{NV}} = -4.6$  mT and  $+6.1$  mT. The orientation of the field changes periodically, in analogy with MFM. Zero-field regions are resolved in the dual iso-B image in Figure 3(e). We observe an area of hundreds of nm<sup>2</sup> with  $B_{\text{NV}} = 0$  mT at the AF domain on the right. Additionally, there is a zero-field line between domains. Since the NV-axis is essentially perpendicular to the sample surface, this zero-field line indicates that there is no field projection along the NV-axis. Therefore, it can be interpreted as the position at which the OOP component of the field is zero, which could define the position of the DW inside the FM stripe.<sup>39,40,43</sup> FM contours with  $B_{\text{NV}} = +6.1$  mT are observed along one side of the zero-field line, while domains with opposite orientation of the field components are periodically separated by the zero-field line as shown in the image in Figure 3(f) for FM domains with  $B_{\text{NV}} = \pm 3.9$  mT.

## Quantitative vector-field maps of a 3D spin texture

Furthermore, we record ODMR maps with a (111)-NV probe as shown in Figure 4(a). The field component projected along the NV-axis is spatially resolved over the sample surface. Given this crystallographic orientation of the tip, we are probing the  $B_z = -B_{\text{NV}}$  component of the stray magnetic field. 2D maps of the in-plane (IP) stray field components can be reconstructed from the experimental map in Figure 4(a) by using the reverse propagation method in Fourier space<sup>51,52</sup> (see section 9 in SI). The obtained  $B_x$  and  $B_y$  stray field maps are depicted in Figure 4(b) and (c), respectively. The maximum value for the static stray field is  $\approx \pm 8.0$  mT at the boundary of the AF domains. The intensity of the stray field

progressively decreases when moving far away from the boundary by hundreds of nm. Both IP and OOP components of the stray field are in the range from hundreds of  $\mu\text{T}$  to 1mT on the AF domains. Even if we expect in a multilayered SAF structure with PMA a full compensation of the magnetization on the AF domains, there will be a small field sensed by the NV above the sample surface due to the different distances between the NV center and each of the FM blocks.<sup>44,53</sup> Additionally, from the images we observe a granular contrast, indicating magnetization variations (see section 10 in SI for a close-up ODMR map on the AF domains). These inhomogeneities or granularity are expected in sputtered multilayered samples with non-uniform thin film thicknesses or atomically flat surface that can induce local variation and non-compensation of the magnetization.

Profiles taken across the region between the AF domains are plotted in Figure 4(g). For simplicity, we define the DW as the region where the OOP field component ( $B_z$ ) is zero<sup>39,40,43</sup> (centred at distance=0 in the profiles). Since it is the region where there is a sign reversal of the stray field (as shown in the dual iso-B results). Note that it strictly corresponds to the actual DW center line ( $m_z = 0$ ,  $z$ -magnetization) only for DWs between two similar domains (AF-AF or FM-FM). Between a FM and an AF domain, however, we only consider the DW on the top FM block. Due to the extended FM stray field, the  $B_z = 0$  line is shifted towards the AF domain compared to the  $m_z = 0$  line. At 75 nm height above the surface, this shift amounts to several tens of nanometers according to our stray field simulation. From the profiles we can also see that above the DW, the IP field components  $B_x$  and  $B_y$  have a local minimum and a maximum, respectively. In contrast to what has been observed in ultra-thin film,<sup>40,43</sup> the profiles of the stray field intensity are not symmetric around the DW. We attribute this to the fact that we are imaging the DW at the top FM block with a collective contribution of the full multilayered structure to the total stray field, in agreement with reported MFM profiles.<sup>12,16</sup> The DW-type can in principle be inferred by fitting the field profiles using an analytical expression of the stray field above the DW under the approximation of a thin sample,<sup>40</sup> i.e. a sample with

magnetic thickness smaller than the sensor-sample distance. This approximation is not valid for the multilayered SAF investigated here since its magnetic thickness is comparable to the NV-sample distance. Previous micromagnetic simulations of multilayered structures demonstrated that FM domains are separated by Néel-type DWs at the top and bottom FM blocks with Bloch-type DWs in the middle of the structure.<sup>17</sup>

Our vector-field maps are in good agreement with micromagnetic simulations. Figures 4(d)-(f) show images obtained from micromagnetic simulation of the stray field components (see methods and section 11 in SI) at a distance of 75 nm from the sample surface, in the range of the estimated  $d_{\text{NV}}$ . From the simulations we observed stray magnetic field of approximately  $\pm 12$  mT. The absolute values of the stray field are higher than the experimental values, suggesting that the magnetic parameters used to initially define the simulated structure need to be optimized as well as the determination of the NV-sample distance. However, the simulated and experimental stray-field maps are qualitatively in good agreement with the stray field values in the same order of magnitude, meaning that the remanent relaxed state achieved in the simulation can describe the magnetic texture of the multilayered SAF. Particularly, the granularity inducing a non-compensated magnetization on the AF domains is also reproduced in the simulated images. The FM domains along the stripe between the two AF domains are also well reproduced by the micromagnetic simulation. To visualize the domain structure in a 2D image, Figure 4(h) displays a transparent overlap of the simulated OOP magnetization of the top and second FM blocks (see section 11 in SI). The FM domains around the DWs are formed due to an alternating left and right lateral shift  $\delta$  between DWs in adjacent FM blocks, leading to a vertical alignment of the magnetic moments along the stacks and giving rise to a 3D spin texture as illustrated in the inset. This lateral shift has been previously reported as driven by the dipolar interaction against the AF-exchange interaction between the FM blocks with a periodic reversal of the FM cores to minimize the magnetostatic energy produced around the DWs, and with a constant DW-shift of  $\delta \approx 20$  nm along the FM stripe between AF domains for a multilayered structure with  $X = 6$  and

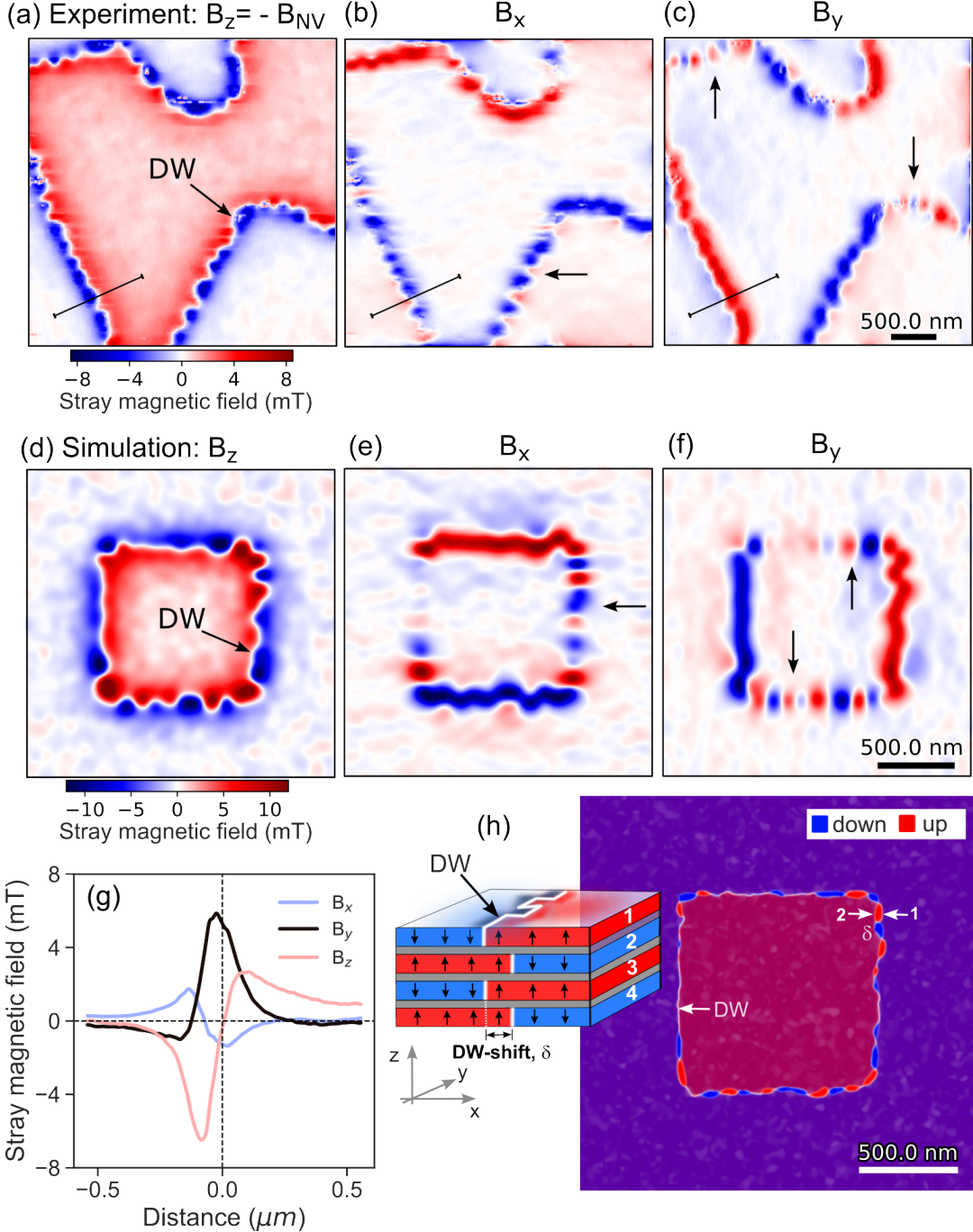


Figure 4: **Stray field maps, DWs and FM cores.** (a) Stray field map of the component projected along the NV-axis,  $B_z = -B_{NV}$ , pixel size of 3.5 nm/px and acquisition time of 100 ms/px. Reconstructed stray field map of the components along (b) the x-axis and (c) the y-axis. Micromagnetic simulated images of the stray field map produced by a square AF domain along (d) the z-axis, (e) the x-axis and (f) the y-axis. Field values are calculated at 75 nm from the sample surface. (g) Profiles of the OOP and IP components of the measured stray fields across the DW. (h) Overlap of the simulated remanent OOP magnetization of the top and second FM blocks to visualize the alternating left and right DW-shift that give rise to the FM cores around the DW with magnetic moments pointing up and down. The inset figure illustrates the 3D magnetic texture of the multilayered structure.

$N = 4$ .<sup>16</sup> In another study, Kiselev *et al.*<sup>15</sup> describe, within their micromagnetic model, that the DW-shift configuration cannot be stabilized only by the interplay between the magnetostatic and the AF-exchange interaction. The stability depends also on DW pinning (grain boundaries, defects or inhomogeneities) that give rise to nucleation sites for one-dimensional FM stripes with fixed width (DW-shift). Remarkably, in the ODMR vector field maps, the periodic modulation of the stray field as a consequence of the DW-shift that reduce the magnetostatic energy is quantitatively and spatially resolved in both the experimental and the simulated IP field maps in Figure 4 (see black arrows). Additionally, the observed granularity or inhomogeneity can favor the stabilization of DW shifts through the DW pinning. We found that the lateral DW-shift is non-uniform along the FM stripes, it varies in the range  $\delta \approx 0 - 40$  nm (see section 11 in SI), generating FM domain cores with different nanometer sizes and wave-shaped DWs.

## Sensing different components of the magnetic noise

Finally, in order to understand the spin dynamics of the magnetic texture in the multilayered SAF, we performed  $T_1$  relaxometry measurements to detect spin noise.  $T_1$  is very sensitive to magnetic fluctuations perpendicular to the NV-axis and with frequencies near the NV resonance frequency.<sup>33</sup> To investigate spin noise, we performed all-optical  $T_1$  measurements<sup>54</sup> using the pulse sequences in Figure 5(a). We use a green laser pulse for initialization of the NV-spin states in  $m_s = 0$ , wait for some time  $\tau$  without laser illumination, and then a second green laser pulse is sent to read out the final spin state. Figure 5(b) shows the  $T_1$  measurements on the (111)-oriented diamond tip. We first measure  $T_1$  before approaching the sample surface, obtaining  $T_1 = (1370 \pm 142) \mu\text{s}$ . This value is expected for diamond tips with shallow NV (nominal implantation depth of 10 nm), where the relaxation time is mostly affected by paramagnetic impurities on the diamond surface.<sup>55</sup> After the sample approach and positioning the tip on the AF domain and then on the FM stripe, we observe a drop in  $T_1$  by almost one and two orders of magnitude, respectively. We obtain  $T_1 = (90 \pm 9) \mu\text{s}$

when the tip is in the AF domain and even shorter  $T_1 = (14 \pm 1) \mu\text{s}$  on the FM stripe. Recent calculations of the spin-wave spectrum in multilayered SAFs<sup>19</sup> predict GHz optical and acoustic spin-wave modes, with the dispersion relation and number of modes dependent on the thickness and number of FM blocks. Additionally, our results are in agreement with the results reported by Finco *et al*<sup>44</sup> on the study of magnetic noise on AF DWs. Thus, we attribute these experimental observations to the presence of magnetic noise in the GHz range, most likely due to thermal magnons with frequencies near the NV spin transition frequency.  $T_1$  is shorter on the FM stripes than on the AF domains, probably due to the confinement of thermal magnonic modes with a stronger noise or frequency that matches the electron spin resonance frequency of the NV at 2.87 GHz.

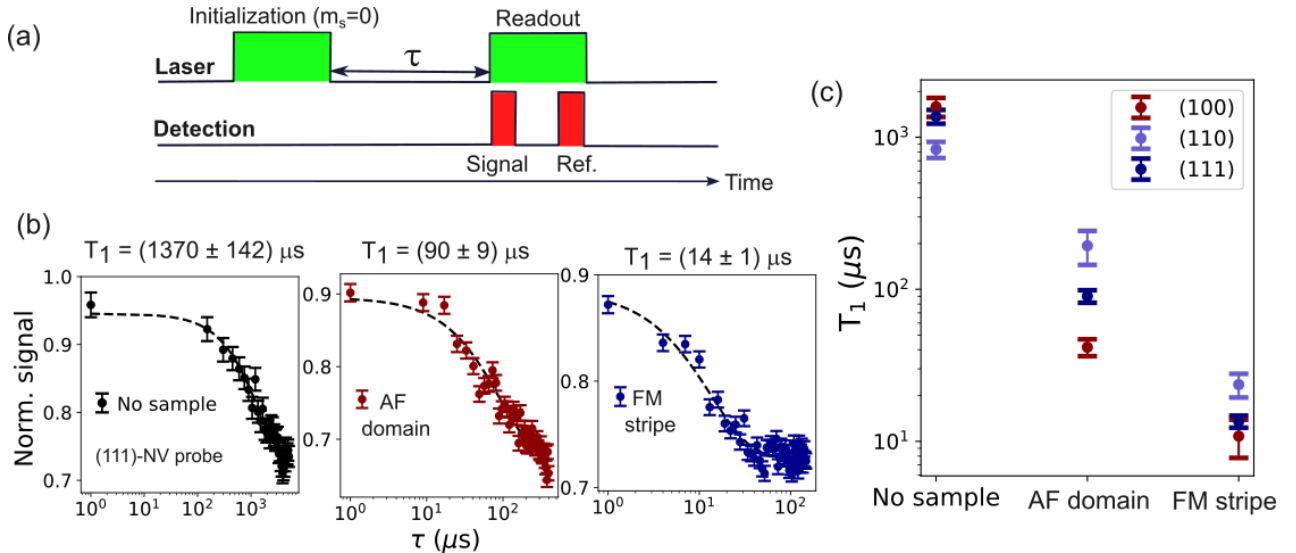


Figure 5:  **$T_1$  relaxometry and magnetic noise** (a) Pulse sequence for all-optical  $T_1$  measurements. A green laser pulse of  $3 \mu\text{s}$  is sent to initially polarize the NV spin state in  $m_s = 0$ , after some time  $\tau$  a second laser pulse is used for reading out the final NV spin state. The signal is read out during a time window of 200 ns (between the first 200-400 ns) of the second pulse and normalized by the signal during the last  $\mu\text{s}$  (reference signal). (b)  $T_1$  measurements performed on a (111)-NV probe with the tip withdrawn from the sample, and after positioning the tip on the AF domain and FM wall. (c) Comparison of  $T_1$  measurements on diamond probes with different crystallographic orientations.

Figure 5(c) shows a comparison of  $T_1$  on NV diamond scanning probes with different crystallographic orientations (see section 12 in SI). The change in  $T_1$  is essentially the same for the

three diamond probes, indicating the existence of magnetic noise with components perpendicular to the respective NV-axis. These  $T_1$  measurements suggest that the PL quenching observed on the FM stripes between AF domains during the acquisition of NV-PL maps could have contributions from both magnetic noise and spin-mixing. For the measurement with the (100)-NV probe, the dominant contribution to the NV-PL quenching comes probably from spin-mixing, as demonstrated by local ODMR measurements. A similar effect is expected for the (110)-NV tip. For the (111)-NV tip, the IP components resolved in the ODMR maps could in principle produce spin mixing. However, there is no evidence of spin-mixing from local ODMR measurements. Hence, the magnetic noise is the dominant contribution that produces quenching in the NV-PL images. Under this condition, it should be possible to observe an improvement in the PL contrast in the NV-PL images when the laser power is decreased below saturation, as observed on samples with AF DW.<sup>44</sup> However, NV-PL quenching images recorded with different laser powers (section 13 in SI) show no improvement in PL contrast, indicating that the field of the FM core along the DW could potentially play a role in the relation between the spin-polarization rate given by the laser power and the spin relaxation rate defined by  $T_1$ .

## Conclusion

In conclusion, we present a detailed study for non-invasive and direct magnetic imaging of complex spin textures in a thick multilayered SAF with PMA using NV-SPM under ambient conditions, with vector-field sensitivity and nanoscale spatial resolution. We demonstrate that qualitative imaging with MFM-like contrast is achieved by applying an off-axis field to introduce a competition of the magnetic field components inducing NV-PL quenching. Quantitative imaging is performed using an NV-probe with the NV-axis aligned with the sample magnetization, reducing possible spin-mixing effects even if the stray field in the sample is on the order of several mT.

Quantitative vector-field maps combined with micromagnetic simulations allow us to explore interlayer coupling effects in the multilayered structure through direct magnetic imaging of DW shifts and the periodic modulation of the IP stray field components produced by the formation of nanometric FM cores around wiggled DWs. These results provide validation on an experimental and micromagnetic simulation level and further insights into existing models about the observed 3D spin texture. Additionally, local  $T_1$  relaxometry measurements reveal the presence of GHz-range magnetic noise on both the AF domains and the DWs with FM cores.

Our findings contribute to the understanding of nanoscale magnetism in complex multilayered SAFs with coexisting AF and FM interactions. Quantitative direct magnetic imaging, along with spin noise sensing, offers new opportunities to investigate mixed spin phases, providing insights into domain and DW stability, interlayer coupling, and spin-wave modes. A proper description of these properties is fundamental for improving existing theoretical models and for designing advanced 3D magnetic architectures.

## Methods

### Sample preparation and characterization

The multilayered SAF was prepared at room temperature by dc magnetron sputtering deposition (ATC 2200 series sputter tool from AJA International, Inc.) with a base pressure of  $8 \cdot 10^{-6}$  Pa, using Ar sputter gas with 0.4 Pa pressure. Si substrates with a thermal 100 nm  $\text{SiO}_2$  layer were used, on which a 1.5 nm thick Ta adhesion layer,<sup>56</sup> 20 nm Pt seed layer for promoting (111) texture,<sup>57</sup> and 3 nm Pt cap against oxidation were deposited.

Hysteresis curve measurements were performed with a Quantum Design MPMS3 superconducting interference device vibrating sample magnetometer (SQUID-VSM).

MFM measurements were performed using a Bruker Dimension Icon Atomic Force Microscope, employing probes model MESP with magnetic Co/Cr coating. All the MFM images

were acquired in the lift imaging mode with tip-sample distance of 15 nm.

## NV-SPM measurements

Qualitative measurements (NV-PL maps and  $T_1$ ) were mostly performed in a new home-built setup, which combines tuning-fork AFM (attocube tip and sample positioner and scanner) with confocal optical microscopy. NV centers in the diamond probes are optically pumped with a 515 nm laser (Toptica, iBEAM-SMART-515-S) and readout by detecting the NV-PL signal after passing through a long-pass 650 nm filter (Thorlabs, FELH0650). The signal is collected by using dual single photon counting modules (Excelitas, SPCM-AQRH-14) mounted in a Hanbury Brown and Twiss geometry for photon autocorrelation measurements. The excitation power of the green laser is 130-300  $\mu$ W, measured after the objective lens (Olympus, MPLFLN100x) that focus (collect) the light on (from) the tip. We use Qzabre quantum scanning tips with sensitivity Q6-Q7 and nominal NV implantation depth of 10 nm. Quantitative measurements (ODMR and dual-iso B) were carried out in a commercial Quantum Scanning NV Microscope (QSM, Qzabre AG) equipped with an electromagnet to apply magnetic field in arbitrary directions. All the NV-SPM images were acquired using the non-contact amplitude modulation mode. The NV-sample distance, as well as, the orientation of the NV-axis in the laboratory frame are determined using the method described in reference,<sup>58</sup> on a 1  $\mu$ m-wide Ta/Pt/Co(0.6nm)/Pt wire with perpendicular magnetic anisotropy as a calibration sample (see SI for more details).

## Micromagnetic simulations

The multilayered SAF was modeled using Mumax<sup>359</sup> with the interlayer exchange interaction implemented as a custom field.<sup>17,60</sup> Four FM blocks with a thickness of 6.75 nm, separated by a 0.75 nm thick spacer, with  $4 \times 4 \times 0.75$  nm<sup>3</sup> cell size, and 8 times lateral periodic boundary conditions were used in the simulation. The structure is initially defined as a perfect square AF domain with a sharp DW (see SI). A relaxation and subsequent minimization was

performed to let the magnetization evolve into the energetic minimum state. The saturation magnetization  $M_s = 833 \text{ kA/m}$  from the SQUID-VSM measurement (see supplementary figure S3) was used; other magnetic parameters were adopted from previous studies in similar multilayer structures: exchange stiffness  $A = 8.0 \text{ pJ/m}$ ,<sup>27</sup> interlayer exchange coupling constant  $A_{\text{IEC}} = -0.7 \text{ mJ/m}^2$ ,<sup>61</sup> perpendicular anisotropy  $K_U = 0.6 \text{ MJ/m}^3$ ,<sup>26</sup> average grain size 32 nm with a normally distributed anisotropy direction variation among the grains.<sup>28</sup> Second-order anisotropy terms and interfacial DMI were not considered in the model.

## Acknowledgement

This work was supported by an Emmy Noether grant from the Deutsche Forschungsgemeinschaft (DFG), project No. 504973613. R.J.P.R and A.S acknowledge financial support by the DFG under the Germany's Excellence Strategy through the Würzburg-Dresden Cluster of Excellence on Complexity and Topology Quantum Matter-ct.qmat (EXC 2174, project-id 390858490). Furthermore, this work was supported by the DFG through the project No. 514946929 at Chemnitz University of Technology.

## References

1. Duine, R. A.; Lee, K.-J.; Parkin, S. S. P.; Stiles, M. D. Synthetic antiferromagnetic spintronics. *Nat. Phys.* **2018**, *14*, 217–219.
2. Wang, K.; Bheemarasetty, V.; Xiao, G. Spin textures in synthetic antiferromagnets: Challenges, opportunities, and future directions. *APL Materials* **2023**, *11*, 070902.
3. Wang, Y.; Zhang, Y.; Li, C.; Wei, J.; He, B.; Xu, H.; Xia, J.; Luo, X.; Li, J.; Dong, J.; He, W.; Yan, Z.; Yang, W.; Ma, F.; Chai, G.; Yan, P.; Wan, C.; Han, X.; Yu, G. Ultra-strong to nearly deep-strong magnon-magnon coupling with a high degree of freedom in synthetic antiferromagnets. *Nat. Commun.* **2024**, *15*, 2077.

4. Xu, T.; Zhou, H.-A.; Dong, Y.; Zhang, Q.; Che, M.; Liu, L.; Wu, Z.; Guan, Z.; Yang, L.; Jiang, W. Fully Compensated Synthetic Antiferromagnets with Pronounced Anomalous Hall and Magneto-Optical Responses. *Phys. Rev. Appl.* **2021**, *16*, 044056.
5. Rong, Y.; Jiang, C.; Wang, H.; Sun, L.; Liu, F.; Lu, J.; Wu, T.; Zhang, Y.; Zhao, Y.; Ma, F.; Mu, Z.; Wang, H.; Yang, Y. Layer-dependent magnon-magnon coupling in a synthetic antiferromagnet. *Phys. Rev. Appl.* **2024**, *21*, 054050.
6. Legrand, W.; Maccariello, D.; Ajejas, F.; Collin, S.; Vecchiola, A.; Bouzehouane, K.; Reyren, N.; Cros, V.; Fert, A. Room-temperature stabilization of antiferromagnetic skyrmions in synthetic antiferromagnets. *Nat. Mater.* **2020**, *19*, 34–42.
7. Pham, V. T.; Sisodia, N.; Di Manici, I.; Urrestarazu-Larrañaga, J.; Bairagi, K.; Pelloux-Prayer, J.; Guedas, R.; Buda-Prejbeanu, L. D.; Auffret, S.; Locatelli, A.; Menteş, T. O.; Pizzini, S.; Kumar, P.; Finco, A.; Jacques, V.; Gaudin, G.; Boulle, O. Fast current-induced skyrmion motion in synthetic antiferromagnets. *Science* **2024**, *384*, 307–312.
8. Godinho, J.; Rout, P. K.; Salikhov, R.; Hellwig, O.; Šobáň, Z.; Otxoa, R. M.; Olejník, K.; Jungwirth, T.; Wunderlich, J. Antiferromagnetic domain wall memory with neuromorphic functionality. *Npj Spintron.* **2024**, *2*.
9. Chen, R.; Cui, Q.; Liao, L.; Zhu, Y.; Zhang, R.; Bai, H.; Zhou, Y.; Xing, G.; Pan, F.; Yang, H.; Song, C. Reducing Dzyaloshinskii-Moriya interaction and field-free spin-orbit torque switching in synthetic antiferromagnets. *Nat. Commun.* **2021**, *12*, 3113.
10. Lonsky, M.; Hoffmann, A. Dynamic fingerprints of synthetic antiferromagnet nanostructures with interfacial Dzyaloshinskii–Moriya interaction. *Journal of Applied Physics* **2022**, *132*, 043903.
11. Hellwig, O.; Kirk, T. L.; Kortright, J. B.; Berger, A.; Fullerton, E. E. A new phase diagram for layered antiferromagnetic films. *Nat. Mater.* **2003**, *2*, 112–116.

12. Hellwig, O.; Berger, A.; Kortright, J. B.; Fullerton, E. E. Domain structure and magnetization reversal of antiferromagnetically coupled perpendicular anisotropy films. *Journal of Magnetism and Magnetic Materials* **2007**, *319*, 13–55.
13. Böhm, B.; Hellwig, O. Tailoring Exchange-Dominated Synthetic Layered Antiferromagnets: From Collective Magnetic Reversal to Exchange Bias. *Small* **2022**, *18*, 2204804.
14. Mouhoub, A.; Millo, F.; Chappert, C.; Kim, J.-V.; Létang, J.; Solignac, A.; Devolder, T. Exchange energies in CoFeB/Ru/CoFeB synthetic antiferromagnets. *Phys. Rev. Mater.* **2023**, *7*, 044404.
15. Kiselev, N. S.; Bran, C.; Wolff, U.; Schultz, L.; Bogdanov, A. N.; Hellwig, O.; Neu, V.; Rößler, U. K. Metamagnetic domains in antiferromagnetically coupled multilayers with perpendicular anisotropy. *Phys. Rev. B* **2010**, *81*, 054409.
16. Hellwig, O.; Berger, A.; Fullerton, E. E. Domain Walls in Antiferromagnetically Coupled Multilayer Films. *Phys. Rev. Lett.* **2003**, *91*, 197203.
17. Salikhov, R.; Samad, F.; Schneider, S.; Pohl, D.; Rellinghaus, B.; Böhm, B.; Ehrler, R.; Lindner, J.; Kiselev, N. S.; Hellwig, O. Multilayer Metamaterials with Ferromagnetic Domains Separated by Antiferromagnetic Domain Walls. *Advanced Electronic Materials* **2025**, *11*, 2400251.
18. Gallardo, R.; Schneider, T.; Chaurasiya, A.; Oelschlägel, A.; Arekapudi, S.; Roldán-Molina, A.; Hübner, R.; Lenz, K.; Barman, A.; Fassbender, J.; Lindner, J.; Hellwig, O.; Landeros, P. Reconfigurable Spin-Wave Nonreciprocity Induced by Dipolar Interaction in a Coupled Ferromagnetic Bilayer. *Phys. Rev. Appl.* **2019**, *12*, 034012.
19. Jiménez-Bustamante, J.; Vidal-Silva, N.; Kákay, A.; Wintz, S.; Gallardo, R. A. Impact of layer count and thickness on spin wave modes in multilayer synthetic antiferromagnets. *Sci. Rep.* **2025**, *15*, 21545.

20. Banerjee, C.; Gruszecki, P.; Klos, J. W.; Hellwig, O.; Krawczyk, M.; Barman, A. Magnonic band structure in a Co/Pd stripe domain system investigated by Brillouin light scattering and micromagnetic simulations. *Phys. Rev. B* **2017**, *96*, 024421.

21. Gruszecki, P.; Banerjee, C.; Mruczkiewicz, M.; Hellwig, O.; Barman, A.; Krawczyk, M. In *Chapter Two - The influence of the internal domain wall structure on spin wave band structure in periodic magnetic stripe domain patterns*; Camley, R. E., Stamps, R. L., Eds.; Solid State Physics; Academic Press, 2021; Vol. 72; pp 29–82.

22. Gubbiotti, G.; Barman, A.; Ladak, S.; Bran, C.; Grundler, D.; Huth, M.; Plank, H.; Schmidt, G.; van Dijken, S.; Streubel, R.; Dobrovolskiy, O.; Scagnoli, V.; Heyderman, L.; Donnelly, C.; Hellwig, O.; Fallarino, L.; Jungfleisch, M. B.; Farhan, A.; Maccaferri, N.; Vavassori, P. *et al.* 2025 roadmap on 3D nanomagnetism. *Journal of Physics: Condensed Matter* **2025**, *37*, 143502.

23. Zhang, K.; Zhernenkov, K.; Saerbeck, T.; Glavic, A.; Qu, L.; Kinane, C. J.; Caruana, A. J.; Hua, E.; Gao, G.; Jin, F.; Ge, B.; Cheng, F.; Pütter, S.; Koutsoubas, A.; Mattauch, S.; Brueckel, T.; Su, Y.; Wang, L.; Wu, W. Soliton-Mediated Magnetic Reversal in an All-Oxide-Based Synthetic Antiferromagnetic Superlattice. *ACS Applied Materials & Interfaces* **2021**, *13*, 20788–20795, PMID: 33877796.

24. Lavrijsen, R.; Lee, J.-H.; Fernández-Pacheco, A.; Petit, D. C. M. C.; Mansell, R.; Cowburn, R. P. Magnetic ratchet for three-dimensional spintronic memory and logic. *Nature* **2013**, *493*, 647–650.

25. Fernández-Pacheco, A.; Steinke, N.-J.; Mahendru, D.; Welbourne, A.; Mansell, R.; Chin, S. L.; Petit, D.; Lee, J.; Dalgliesh, R.; Langridge, S.; Cowburn, R. P. Magnetic State of Multilayered Synthetic Antiferromagnets during Soliton Nucleation and Propagation for Vertical Data Transfer. *Advanced Materials Interfaces* **2016**, *3*, 1600097.

26. Koch, L.; Samad, F.; Lenz, M.; Hellwig, O. Manipulating the Energy Balance of

Perpendicular-Anisotropy Synthetic Antiferromagnets by He+-Ion Irradiation. *Phys. Rev. Appl.* **2020**, *13*, 024029.

27. Salikhov, R.; Samad, F.; Böhm, B.; Schneider, S.; Pohl, D.; Rellinghaus, B.; Ullrich, A.; Albrecht, M.; Lindner, J.; Kiselev, N. S.; Hellwig, O. Control of Stripe-Domain-Wall Magnetization in Multilayers Featuring Perpendicular Magnetic Anisotropy. *Phys. Rev. Appl.* **2021**, *16*, 034016.
28. Salikhov, R.; Samad, F.; Arekapudi, S. S. P. K.; Ehrler, R.; Lindner, J.; Kiselev, N. S.; Hellwig, O. Control and tunability of magnetic bubble states in multilayers with strong perpendicular magnetic anisotropy at ambient conditions. *Phys. Rev. B* **2022**, *106*, 054404.
29. Balasubramanian, G.; Chan, I. Y.; Kolesov, R.; Al-Hmoud, M.; Tisler, J.; Shin, C.; Kim, C.; Wojcik, A.; Hemmer, P. R.; Krueger, A.; Hanke, T.; Leitenstorfer, A.; Bratschitsch, R.; Jelezko, F.; Wrachtrup, J. Nanoscale imaging magnetometry with diamond spins under ambient conditions. *Nature* **2008**, *455*, 648–651.
30. Stepanova, M.; Masell, J.; Lysne, E.; Schoenherr, P.; Köhler, L.; Paulsen, M.; Qaiumzadeh, A.; Kanazawa, N.; Rosch, A.; Tokura, Y.; Brataas, A.; Garst, M.; Meier, D. Detection of Topological Spin Textures via Nonlinear Magnetic Responses. *Nano Letters* **2022**, *22*, 14–21, PMID: 34935368.
31. Zelent, M.; Vetrova, I. V.; Šoltýs, J.; Li, X.; Zhou, Y.; Gubanov, V. A.; Sadovnikov, A. V.; Šcepka, T.; Dérer, J.; Stoklas, R.; Cambel, V.; Mruczkiewicz, M. Skyrmion Formation in Nanodisks Using Magnetic Force Microscopy Tip. *Nanomaterials* **2021**, *11*.
32. Casiraghi, A.; Corte-León, H.; Vafaee, M.; Garcia-Sánchez, F.; Durin, G.; Pasquale, M.; Jakob, G.; Kläui, M.; Kazakova, O. Individual skyrmion manipulation by local magnetic field gradients. *Commun. Phys.* **2019**, *2*.

33. Degen, C. L.; Reinhard, F.; Cappellaro, P. Quantum sensing. *Rev. Mod. Phys.* **2017**, *89*, 035002.

34. Finco, A.; Jacques, V. Single spin magnetometry and relaxometry applied to antiferromagnetic materials. *APL Materials* **2023**, *11*, 100901.

35. Rovny, J.; Gopalakrishnan, S.; Jayich, A. C. B.; Maletinsky, P.; Demler, E.; de Leon, N. P. Nanoscale diamond quantum sensors for many-body physics. *Nat. Rev. Phys.* **2024**, *6*, 753–768.

36. Budakian, R.; Finkler, A.; Eichler, A.; Poggio, M.; Degen, C. L.; Tabatabaei, S.; Lee, I.; Hammel, P. C.; Eugene, S. P.; Taminiau, T. H.; Walsworth, R. L.; London, P.; Bleszynski Jayich, A.; Ajoy, A.; Pillai, A.; Wrachtrup, J.; Jelezko, F.; Bae, Y.; Heinrich, A. J.; Ast, C. R. *et al.* Roadmap on nanoscale magnetic resonance imaging. *Nanotechnology* **2024**, *35*, 412001.

37. Christensen, D. V.; Staub, U.; Devidas, T. R.; Kalisky, B.; Nowack, K. C.; Webb, J. L.; Andersen, U. L.; Huck, A.; Broadway, D. A.; Wagner, K.; Maletinsky, P.; van der Sar, T.; Du, C. R.; Yacoby, A.; Collomb, D.; Bending, S.; Oral, A.; Hug, H. J.; Mandru, A.-O.; Neu, V. *et al.* 2024 roadmap on magnetic microscopy techniques and their applications in materials science. *Journal of Physics: Materials* **2024**, *7*, 032501.

38. Xu, Z.; Palm, M. L.; Huxter, W.; Herb, K.; Abendroth, J. M.; Bouzehouane, K.; Boulle, O.; Gabor, M. S.; Urrestarazu Larranaga, J.; Morales, A.; Rhensius, J.; Puebla-Hellmann, G.; Degen, C. L. Minimizing Sensor-Sample Distances in Scanning Nitrogen-Vacancy Magnetometry. *ACS Nano* **2025**, *19*, 8255–8265, PMID: 39983234.

39. Tetienne, J.-P.; Hingant, T.; Rondin, L.; Rohart, S.; Thiaville, A.; Jué, E.; Gaudin, G.; Roch, J.-F.; Jacques, V. Nitrogen-vacancy-center imaging of bubble domains in a 6-Å film of cobalt with perpendicular magnetization. *Journal of Applied Physics* **2014**, *115*, 17D501.

40. Tetienne, J.-P.; Hingant, T.; Martínez, L. J.; Rohart, S.; Thiaville, A.; Diez, L. H.; Garcia, K.; Adam, J.-P.; Kim, J.-V.; Roch, J.-F.; Miron, I. M.; Gaudin, G.; Vila, L.; Ocker, B.; Ravelosona, D.; Jacques, V. The nature of domain walls in ultrathin ferromagnets revealed by scanning nanomagnetometry. *Nat. Commun.* **2015**, *6*, 6733.

41. Gross, I.; Martínez, L. J.; Tetienne, J.-P.; Hingant, T.; Roch, J.-F.; Garcia, K.; Soucaille, R.; Adam, J. P.; Kim, J.-V.; Rohart, S.; Thiaville, A.; Torrejon, J.; Hayashi, M.; Jacques, V. Direct measurement of interfacial Dzyaloshinskii-Moriya interaction in  $X|\text{CoFeB}|\text{MgO}$  heterostructures with a scanning NV magnetometer ( $X = \text{Ta, TaN, and W}$ ). *Phys. Rev. B* **2016**, *94*, 064413.

42. Tetienne, J.-P.; Hingant, T.; Kim, J.-V.; Diez, L. H.; Adam, J.-P.; Garcia, K.; Roch, J.-F.; Rohart, S.; Thiaville, A.; Ravelosona, D.; Jacques, V. Nanoscale imaging and control of domain-wall hopping with a nitrogen-vacancy center microscope. *Science* **2014**, *344*, 1366–1369.

43. McLaughlin, N. J.; Li, S.; Brock, J. A.; Zhang, S.; Lu, H.; Huang, M.; Xiao, Y.; Zhou, J.; Tserkovnyak, Y.; Fullerton, E. E.; Wang, H.; Du, C. R. Local Control of a Single Nitrogen-Vacancy Center by Nanoscale Engineered Magnetic Domain Wall Motion. *ACS Nano* **2023**, *17*, 25689–25696, PMID: 38050827.

44. Finco, A.; Haykal, A.; Tanos, R.; Fabre, F.; Chouaieb, S.; Akhtar, W.; Robert-Philip, I.; Legrand, W.; Ajejas, F.; Bouzehouane, K.; Reyren, N.; Devolder, T.; Adam, J.-P.; Kim, J.-V.; Cros, V.; Jacques, V. Imaging non-collinear antiferromagnetic textures via single spin relaxometry. *Nat. Commun.* **2021**, *12*, 767.

45. Finco, A.; Kumar, P.; Pham, V. T.; Urrestarazu-Larrañaga, J.; Garcia, R. G.; Rollo, M.; Boulle, O.; Kim, J.-V.; Jacques, V. Thermal Spin Wave Noise as a Probe for the Dzyaloshinskii-Moriya Interaction. *Phys. Rev. Lett.* **2025**, *135*, 136703.

46. Welter, P.; Rhensius, J.; Morales, A.; Wörnle, M. S.; Lambert, C.-H.; Puebla-

Hellmann, G.; Gambardella, P.; Degen, C. L. Scanning nitrogen-vacancy center magnetometry in large in-plane magnetic fields. *Applied Physics Letters* **2022**, *120*, 074003.

47. Rohner, D.; Happacher, J.; Reiser, P.; Tschudin, M. A.; Tallaire, A.; Achard, J.; Shields, B. J.; Maletinsky, P. (111)-oriented, single crystal diamond tips for nanoscale scanning probe imaging of out-of-plane magnetic fields. *Applied Physics Letters* **2019**, *115*, 192401.

48. Tetienne, J.-P.; Rondin, L.; Spinicelli, P.; Chipaux, M.; Debuisschert, T.; Roch, J.-F.; Jacques, V. Magnetic-field-dependent photodynamics of single NV defects in diamond: an application to qualitative all-optical magnetic imaging. *New Journal of Physics* **2012**, *14*, 103033.

49. Rollo, M.; Finco, A.; Tano, R.; Fabre, F.; Devolder, T.; Robert-Philip, I.; Jacques, V. Quantitative study of the response of a single NV defect in diamond to magnetic noise. *Phys. Rev. B* **2021**, *103*, 235418.

50. Rondin, L.; Tetienne, J.-P.; Hingant, T.; Roch, J.-F.; Maletinsky, P.; Jacques, V. Magnetometry with nitrogen-vacancy defects in diamond. *Reports on Progress in Physics* **2014**, *77*, 056503.

51. Lima, E. A.; Weiss, B. P. Obtaining vector magnetic field maps from single-component measurements of geological samples. *Journal of Geophysical Research: Solid Earth* **2009**, *114*.

52. Dovzhenko, Y.; Casola, F.; Schlotter, S.; Zhou, T. X.; Büttner, F.; Walsworth, R. L.; Beach, G. S.; Yacoby, A. Magnetostatic twists in room-temperature skyrmions explored by nitrogen-vacancy center spin texture reconstruction. *Nature communications* **2018**, *9*, 2712.

53. Kiselev, N. S.; Dragunov, I. E.; Neu, V.; Rößler, U. K.; Bogdanov, A. N. Theoretical

analysis of magnetic force microscopy contrast in multidomain states of magnetic superlattices with perpendicular anisotropy. *Journal of Applied Physics* **2008**, *103*, 043907.

54. Levine, E. V.; Turner, M. J.; Kehayias, P.; Hart, C. A.; Langellier, N.; Trubko, R.; Glenn, D. R.; Fu, R. R.; Walsworth, R. L. Principles and techniques of the quantum diamond microscope. *Nanophotonics* **2019**, *8*, 1945–1973.

55. Rosskopf, T.; Dussaux, A.; Ohashi, K.; Loretz, M.; Schirhagl, R.; Watanabe, H.; Shikata, S.; Itoh, K. M.; Degen, C. L. Investigation of Surface Magnetic Noise by Shallow Spins in Diamond. *Phys. Rev. Lett.* **2014**, *112*, 147602.

56. Ehrler, R.; Uhlig, T.; Hübner, R.; Samad, F.; Heinig, P.; Hellwig, O. Manifold role of a Ta adhesion layer in pressure-tuned Co/Pt multilayers. *Phys. Rev. B* **2025**, *112*, 094452.

57. Zeper, W. B.; van Kesteren, H. W.; Jacobs, B. A. J.; Spruit, J. H. M.; Garcia, P. F. Hysteresis, microstructure, and magneto-optical recording in Co/Pt and Co/Pd multilayers. *Journal of Applied Physics* **1991**, *70*, 2264–2271.

58. Hingant, T.; Tetienne, J.-P.; Martínez, L. J.; Garcia, K.; Ravelosona, D.; Roch, J.-F.; Jacques, V. Measuring the Magnetic Moment Density in Patterned Ultrathin Ferromagnets with Submicrometer Resolution. *Phys. Rev. Appl.* **2015**, *4*, 014003.

59. Vansteenkiste, A.; Leliaert, J.; Dvornik, M.; Helsen, M.; Garcia-Sanchez, F.; Van Waeyenberge, B. The design and verification of MuMax3. *AIP Advances* **2014**, *4*, 107133.

60. Joos, J. J.; Bassirian, P.; Gypens, P.; Mulders, J.; Litzius, K.; Van Waeyenberge, B.; Leliaert, J. Tutorial: Simulating modern magnetic material systems in mumax3. *Journal of Applied Physics* **2023**, *134*, 171101.

61. Samad, F.; Hlawacek, G.; Arekapudi, S. S. P. K.; Xu, X.; Koch, L.; Lenz, M.; Hellwig, O.

Controlled and deterministic creation of synthetic antiferromagnetic domains by focused ion beam irradiation. *Applied Physics Letters* **2021**, *119*, 022409.

# Supplementary information: Nanoscale magnetometry of a synthetic three-dimensional spin texture

Ricardo Javier Peña Román,<sup>\*,†,‡,¶</sup> Sandip Maity,<sup>†,‡</sup> Fabian Samad,<sup>§,||</sup> Dinesh Pinto,<sup>†,⊥</sup> Simon Josephy,<sup>#</sup> Andrea Morales,<sup>#</sup> Attila Kákay,<sup>§</sup> Klaus Kern,<sup>†,⊥</sup> Olav Hellwig,<sup>§,||</sup> and Aparajita Singha<sup>\*,†,‡,¶</sup>

<sup>†</sup>*Max Planck Institute for Solid State Research, 70569 Stuttgart, Germany*

<sup>‡</sup>*Institute of Solid State and Materials Physics, Dresden University of Technology, 01069 Dresden, Germany*

<sup>¶</sup>*Würzburg-Dresden Cluster of Excellence ct.qmat, 01069 Dresden, Germany*

<sup>§</sup>*Institute of Ion Beam Physics and Materials Research, Helmholtz-Zentrum Dresden-Rossendorf, 01328 Dresden, Germany*

<sup>||</sup>*Institute of Physics, Chemnitz University of Technology, 09107 Chemnitz, Germany*

<sup>⊥</sup>*Institute de Physique, Ecole Polytechnique Fédérale de Lausanne, CH-1015 Lausanne, Switzerland*

<sup>#</sup>*QZabre AG, 8050 Zurich, Switzerland*

E-mail: ricardo.pena\_roman@tu-dresden.de; aparajita.singha@tu-dresden.de

## Section 1: Characterization of the NV-diamond probes

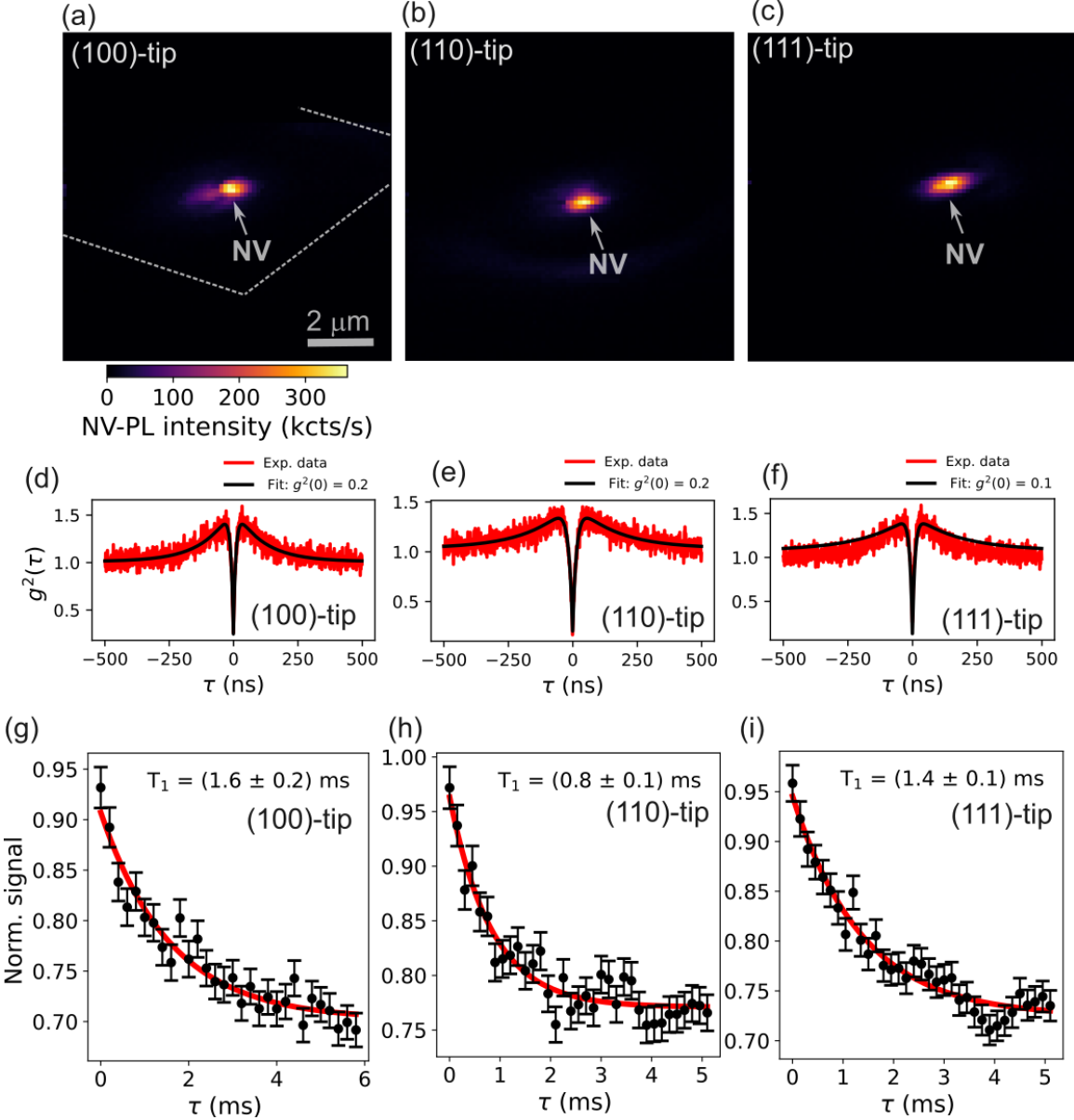


Figure S1: Pre-characterization of commercial NV-probes. (a)-(c) confocal images, (d)-(f) photon autocorrelation and (e)-(f)  $T_1$  measurements on (100), (110) and (111) NV-probes before approaching the sample. Green laser (515 nm) power of 130-300  $\mu$ W.

We used commercial scanning tips (Qzabre, Q6-Q7) with (100)-, (110)-, and (111)-oriented diamond crystals. Before approaching the sample to the tip and scanning, all tips are pre-characterized by confocal imaging, photon autocorrelation, and  $T_1$  measurements. Figures S1(a)-(c) show confocal images acquired with a green 515 nm laser using excitation power

of 130-300  $\mu\text{W}$ . Most of the light comes from the NV center, which appears as a bright spot with a signal above 300 kcts/s. The signal from the diamond base plate is weaker and not visible in the image. For reference, it is indicated by the white dashed line around the bright spot in panel (a). Figures S1(d)-(f) show the respective photon autocorrelation,  $g^2(\tau)$ , measurements where  $g^2(0) < 0.5$  confirms that there is a single NV defect in every tip. Additionally, Figures S1(g)-(i) show  $T_1$  measurements acquired using the pulse sequence described in the main text. The results indicate that these commercial tips with a nominal implantation depth of 10 nm exhibit longitudinal spin relaxation times of 0.8-1.4 ms. These  $T_1$  data are plotted in Figure 5(c) of the main text.

## Section 2: Calibration of the NV-sample distance

For quantitative measurements and comparison of data acquired with different scanning probes, it is essential to characterize the sensor-sample distance and the orientation of the single NV-spin. We used the conventional method described in the reference,<sup>1</sup> in which the stray field produced at the edges of a thin FM wire is corrected considering the topography profile and fitted by an analytical expression. As illustrated in Figure S2(a), for an FM wire along the y-axis, with thickness  $t$ , width  $W$ , and left and right edges at the positions  $x_L$  and  $x_R$ , respectively, the field at the distance  $d \gg t$  and position  $x$  is given by:

$$\begin{aligned}
\vec{B}^{wire}(x, 0, d) &= \vec{B}^{edge}(x - x_L, 0, d) + \vec{B}^{edge}(x - x_R, 0, d) \\
&= \frac{\mu_0 I_s}{2\pi} W \left[ d \left( \frac{w + 2(x_L - x)}{[(x - x_L)^2 + d^2][(x - x_R)^2 + d^2]} \right) \hat{e}_x + \left( \frac{x^2 + xw - 2xx_R + x_L x_R - wd^2}{[(x - x_L)^2 + d^2][(x - x_R)^2 + d^2]} \right) \hat{e}_z \right] \\
&= B_x^{wire}(x, 0, d) \hat{e}_x + B_z^{wire}(x, 0, d) \hat{e}_z
\end{aligned} \tag{1}$$

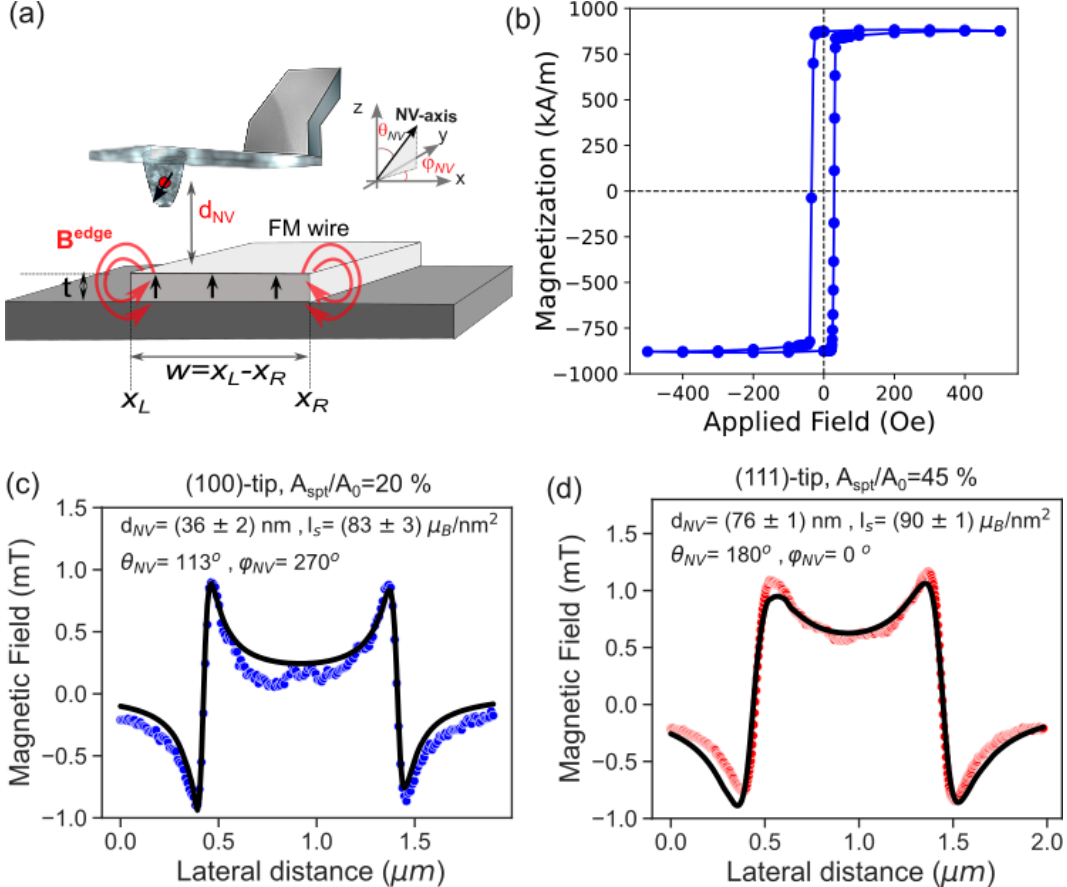


Figure S2: **Calibration sample and determination of the NV-sample distance.** (a) Schematic of the scanning probe and the stray field of a thin FM wire. We assume the wire parallel to the y-axis, and with magnetic thickness  $t \approx 1 \text{ nm}$ . The distance  $d_{NV}$  is determined from the sample surface and along the z-axis. The angles  $(\theta_{NV}, \varphi_{NV})$  determine the orientation of the NV-axis in the laboratory frame. (b) out-of-plane hysteresis curve of the calibration sample. (c) Fitting of the stray field profile measured across the wire with the (100)-NV tip and (d) with the (111)-NV tip. The fits are shown in solid black curves and the results as inset.

where  $I_s = M_s t$ , is the surface density of magnetic moments with  $M_s$  the saturation magnetization. The field sensed by the NV center is given by the projection of  $\vec{B}^{wire}(x, 0, d)$  along the NV-axis defined by the unit vector  $\hat{e}_{NV} = \cos \varphi_{NV} \sin \theta_{NV} \hat{e}_x + \sin \varphi_{NV} \sin \theta_{NV} \hat{e}_y + \cos \theta_{NV} \hat{e}_z$ , with the angles  $\varphi_{NV} \in [0^\circ, 360^\circ]$  and  $\theta_{NV} \in [0^\circ, 180^\circ]$ . Therefore, the field measured by the scanning-NV tip is:

$$B_{NV}(x, 0, d + \delta d) = B_x^{wire}(x, 0, d + \delta d) \cos \varphi_{NV} \sin \theta_{NV} + B_z^{wire}(x, 0, d + \delta d) \cos \theta_{NV} \quad (2)$$

The substitution  $d \rightarrow d + \delta d$  is introduced to include topography variations and measure the sensor-sample distance from the wire surface (topography correction).

We use as a calibration sample a FM wire of Ta/Pt/Co(0.6nm)/Pt deposited on a SiO<sub>2</sub>/Si substrate. The width of the wire is around 1  $\mu\text{m}$ , and the magnetic thickness is considered to be  $t \approx 1$  nm (0.6 nm (Co) + 2\*0.2 nm (Pt)). We assume 0.2 nm of Pt on both sides of the Co layer to contribute to the magnetic moment. Note that this value is not critical since  $I_s = M_s t$  is the relevant parameter and not  $M_s$  and  $t$  separately. The OOP hysteresis curve of the calibration sample is shown in Figure S2(b), from which we obtain an OOP saturation magnetization  $M_s = (884 \pm 88)$  kA/m. From here, we calculate  $I_s = (95 \pm 10)$   $\mu_B/\text{nm}^2$ . Stray field profiles measured across the FM wire with (100)- and (111)-NV probes are shown in Figure S2(c) and (d), respectively. The profiles are fitted using the expression in equation (2), and the results are presented as insets in the figures. We performed scanning using the amplitude modulation mode. The profile acquired with the (100)-probe was recorded using an amplitude setpoint ( $A_{stp}$ ) of 20% of the amplitude of the scanning tip in free space ( $A_0$ ). For calibration with a (111) probe the amplitude setpoint was set to  $A_{stp}/A_0 = 45\%$ , for which we obtain a higher NV-sample distance. The values for  $I_s$  obtained from the fitting are in good agreement with the experimental value. All the images recorded on the multilayered SAFs were acquired with similar scanning parameters to the calibration sample. Therefore, we expect the NV-sample distance to be in the range of 36-76 nm.

### **Section 3: Saturation magnetization and MFM images**

Figure S3(a) shows the OOP hysteresis curve measured at 300 K on the multilayered SAFs described in the main text. As represented in the figure, we observed four discrete steps in the loop, corresponding to the magnetic reversal of each of the FM blocks. The absolute total saturation magnetization is  $M_s = (833 \pm 83)$  kA/m, for configurations with a full magnetization pointing up/down. Figure S3(b) shows a large area MFM image, after saturation

with an IP field. The magnetic texture consists of large AF domains with periodic contrast along the FM stripes at the AF domain boundaries. A high-resolution MFM image is shown in Figure S3(c). Figure S3(d) shows profiles taken across and along a FM stripe. We estimate a FM stripe width of around 100 nm and a local periodicity of the contrast of 300 nm. In agreement with the observations by Hellwig *et al.*,<sup>2</sup> the non-zero integrated area of the profiles across the stripe demonstrate FM order.

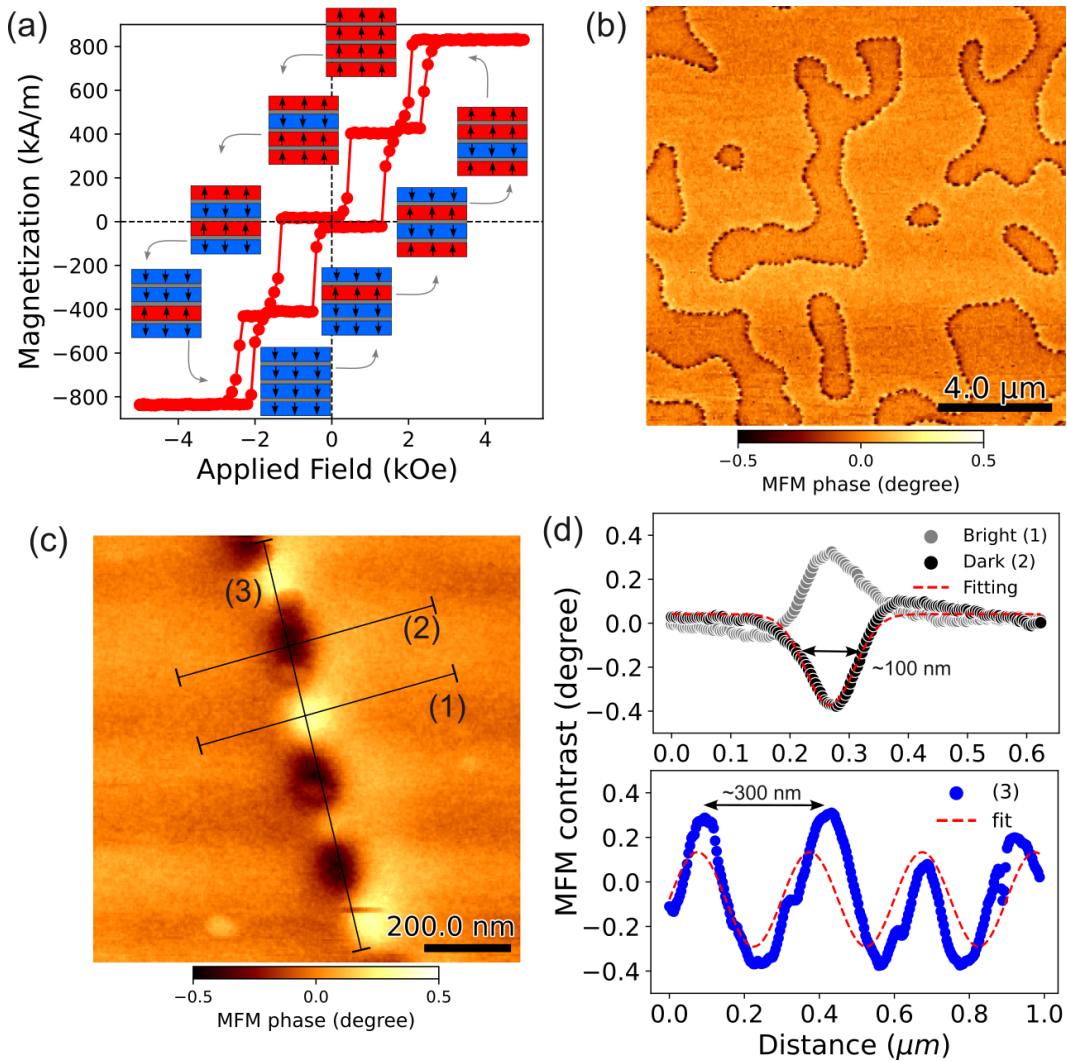


**Figure S3: Hysteresis curve and FM DW profiles.** (a) Out-of-plane hysteresis loop. (b) large area MFM image, 15  $\mu\text{m}$  x 15  $\mu\text{m}$ . (c) High resolution MFM image (1  $\mu\text{m}$  x 1  $\mu\text{m}$ ) of the periodic contrast along the FM stripe at the AF domain boundary. (d) MFM profiles across and along the FM stripe. The FM stripe width and periodicity are estimated by fitting the profiles to a gaussian and sinusoidal function, respectively.

## Section 4: Additional ODMR measurements with the (100)-NV probe

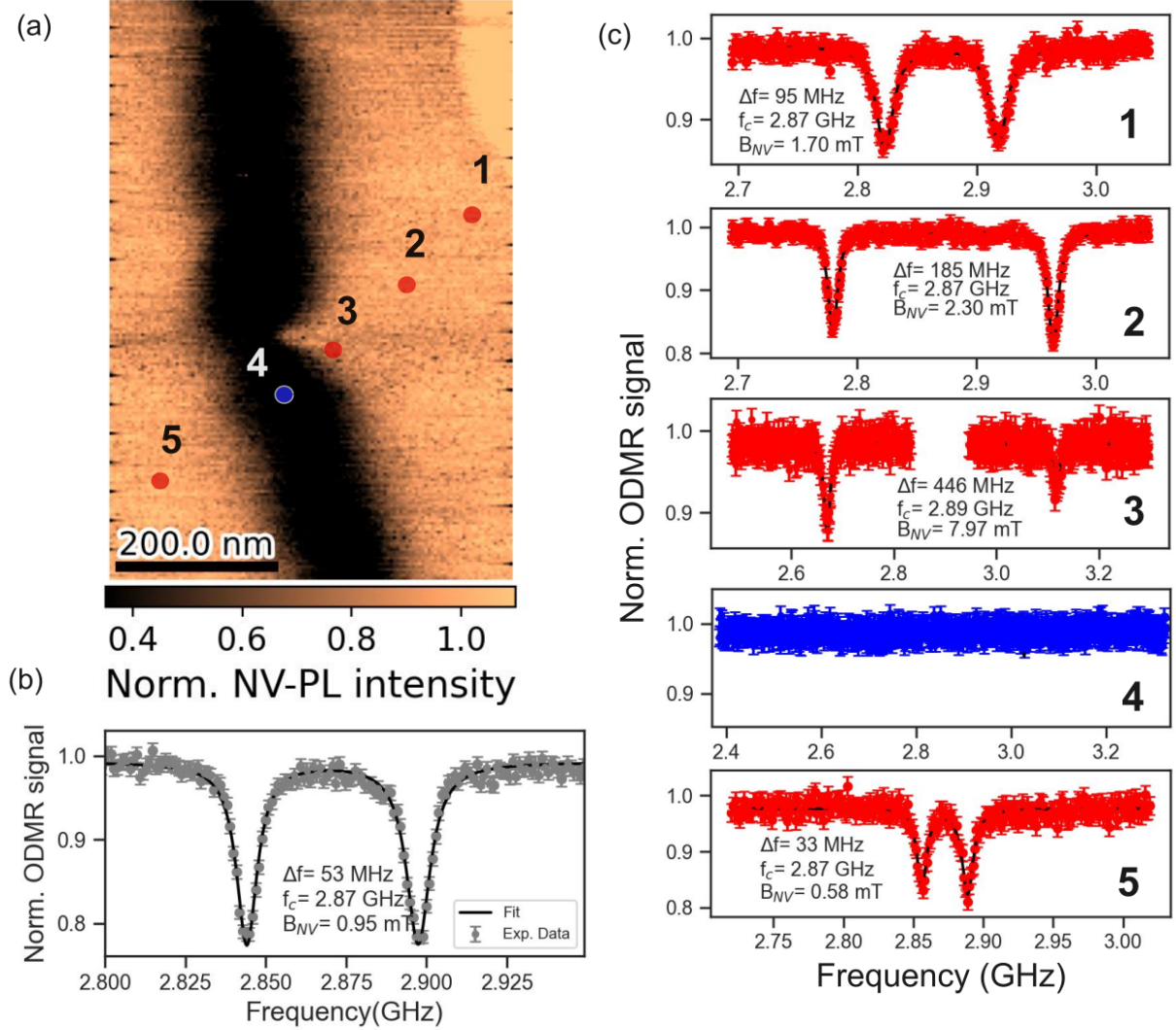


Figure S4: **Local ODMR measurements.** (a) NV-PL quenching map. (b) ODMR spectrum of the tip before approaching the sample. (c) ODMR spectra measured locally after approaching the sample and positioning the tip on the locations indicated in (a). The inset parameters in every plot correspond to the splitting ( $\Delta f$ ), the central frequency ( $f_c$ ), and the field sensed by the NV-center ( $B_{NV}$ ).

In Figure S4, we present ODMR measurements in addition to those shown in Figure 2 of the main text. In Figure S4(a), a high-resolution NV-PL quenching image is shown, recorded without applying any off-axis field to the NV sensor. In Figure S4(b) we observe

the ODMR spectrum of the tip before approaching the sample. The spectrum was acquired after turning off the electromagnet used to apply the external field. There is still a remnant external field that can be sensed by the NV, which gives rise to the initial splitting observed in the spectrum. Figure S4(c) shows ODMR spectra measured locally across the FM stripe between AF domains and at the positions 1-5 indicated in Figure S4(a). Close to the FM stripe, at position 3, the Zeeman shift is not symmetric with respect to  $f_0$ ; the central frequency is shifted from 2.87 GHz to 2.89 GHz. As discussed in the main text, it is an indication of spin-mixing induced by off-axis field components on the FM stripe. For some tip locations, the field is too strong, and it is not possible to see any splitting within the measured frequency range, as in the case of the spectrum measured at location 4.

## Section 5: NV-PL quenching and MFM-like contrast

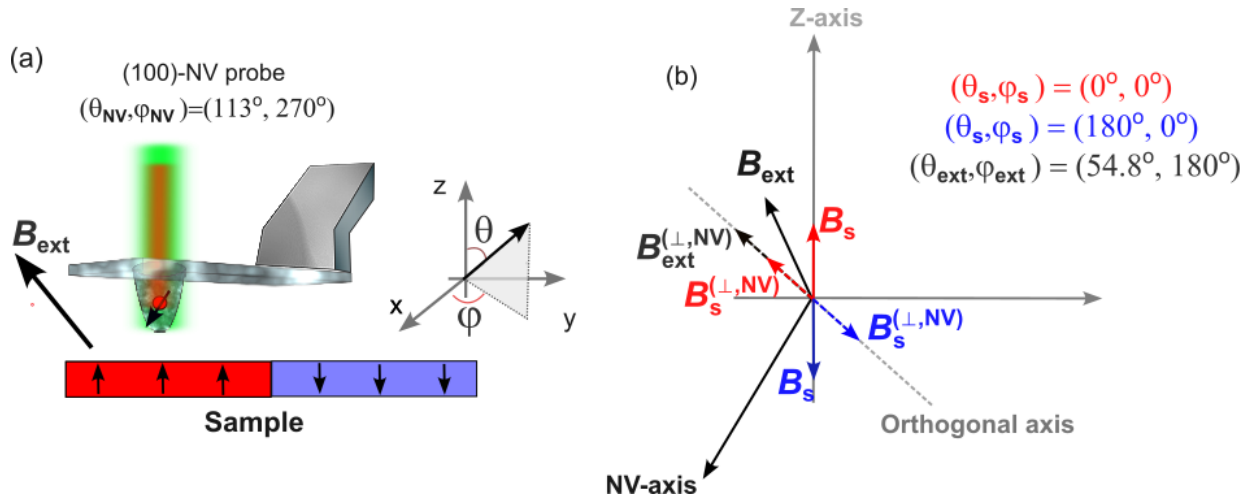


Figure S5: **Magnetic field components perpendicular to the NV-axis.** (a) schematic illustration of the (100)-NV tip scanning domains with magnetic moments pointing up and down. (b) Projection of the field components along the NV-axis.

During the acquisition of NV-PL quenching images in the presence of an off-axis field, the sensor will experience a total field with contributions from both the sample stray field and the field applied externally. Each contribution is described by the vector:

$$\vec{B}_i = B_i \langle \sin \theta_i \sin \varphi_i, \sin \theta_i \cos \varphi_i, \cos \theta_i \rangle \quad (3)$$

with  $i = s, \text{ext}$ , for the sample and external field, respectively. The parallel and perpendicular projections on the NV-axis are given by

$$B_i^{(\parallel, \text{NV})} = \vec{B}_i \cdot \hat{e}_{\text{NV}}, \text{ and } B_i^{(\perp, \text{NV})} = \left\| \vec{B}_i - \vec{B}_i^{(\parallel, \text{NV})} \right\| \quad (4)$$

As described in the main text, the quenching in the PL of the NV is mainly produced by spin-mixing effects induced by components of the field that are perpendicular to the NV-axis. Thus, the total field perpendicular to the NV-axis is given by the field compensation  $\mathbf{B}_{\text{total}}^{(\perp, \text{NV})} = \mathbf{B}_{\text{ext}}^{(\perp, \text{NV})} + \mathbf{B}_s^{(\perp, \text{NV})}$ . Table S1 summarizes the magnitude of the total OOP component of the field on domains with magnetization pointing up ( $\uparrow$ ) and down ( $\downarrow$ ), and the relative contrast between bright and dark areas in NV-PL images acquired at different values of the external applied field.

Table S1: Relative contrast between bright and dark areas in NV-PL quenching maps

$B_{\text{ext}}$ [mT]	$B_{\text{total}\uparrow}^{(\perp, \text{NV})}$ [mT]	$B_{\text{total}\downarrow}^{(\perp, \text{NV})}$ [mT]	$C$ [%]
0	5	5	0
20	24	15	23
25	29	20	18
40	44	34	13
60	63	54	7

**Section 6: Additional NV-PL maps with the (100)-NV probe on a sample with N=17, X=7.**

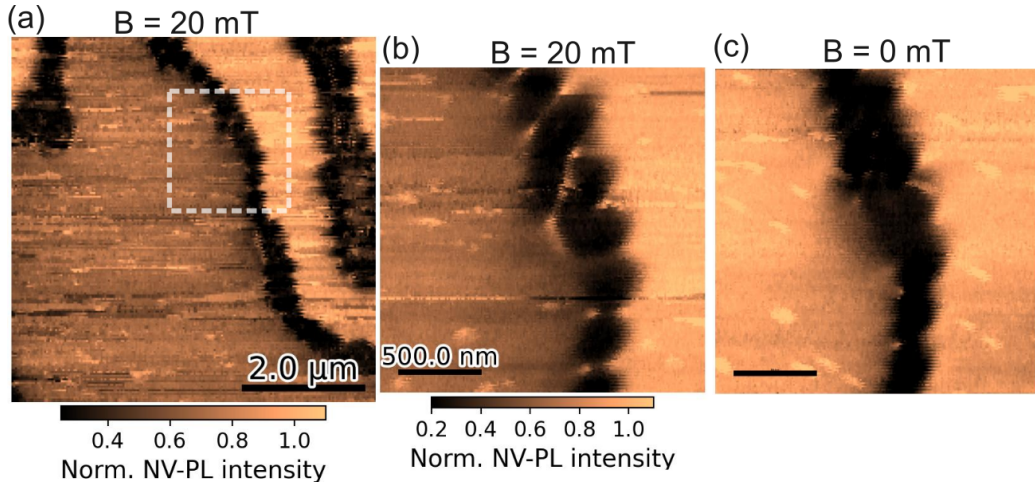


Figure S6: **NV-PL images with MFM-like contrast**. (a) NV-PL image of the sample  $[[\text{Co}(0.55\text{nm})/\text{Pt}(0.70\text{nm})]_6/\text{Co}(0.55\text{nm})/\text{Ru}(0.75\text{nm})]_{16}/[\text{Co}(0.55\text{nm})/\text{Pt}(0.70\text{nm})]_7$ , acquired with an external off-axis field of 20 mT. NV-PL images of the same area recorded (b) with and (c) without applying an off-axis field.

MFM-like contrast in NV-PL images is consistently observed when an off-axis field is applied to the NV during scanning. Figure S6 presents additional data acquired in a different sample. Figure S6(a) shows an NV-PL quenching images recorded on the sample  $[[\text{Co}(0.55\text{nm})/\text{Pt}(0.70\text{nm})]_6/\text{Co}(0.55\text{nm})/\text{Ru}(0.75\text{nm})]_{16}/[\text{Co}(0.55\text{nm})/\text{Pt}(0.70\text{nm})]_7$ , when applying an off-axis field of 20 mT in the direction  $(\theta_{\text{ext}}, \varphi_{\text{ext}}) = (54.8^\circ, 180^\circ)$ . There is strong quenching along the FM stripe, as well as a slight difference in the PL contrast between left and right AF domain. From Figures S6(b) and (c), it can be seen that the quenching along the FM stripe is uniform after turning the external field off, and the PL contrast at the AF domains is the same.

## Section 7: Additional ODMR measurements a with the (111)-NV probe

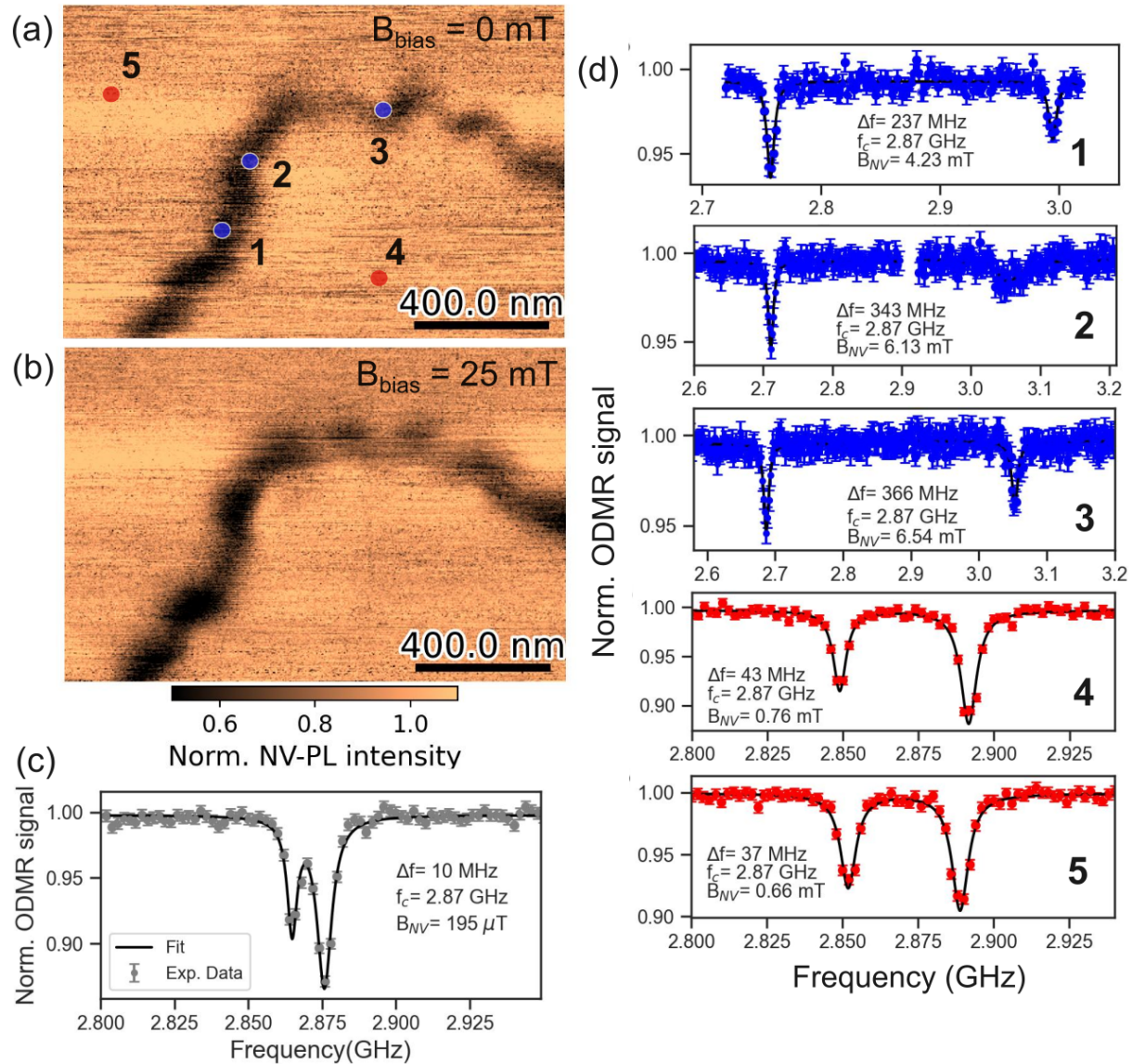


Figure S7: **Local ODMR measurements.** NV-PL quenching map (a) without and (b) with bias field along the NV-axis. (c) ODMR spectrum of the tip before approaching the sample. (c) ODMR spectra measured locally after approaching the sample and positioning the tip on the locations indicated in (a). The inset parameters in every plot correspond to the splitting ( $\Delta f$ ), the central frequency ( $f_c$ ), and the field sensed by the NV-center ( $B_{NV}$ ).

NV-PL quenching images recorded with the (111)-NV tip and acquired with and without an applied bias field are shown in Figure S7(a) and S7(b), respectively. The bias field, which is necessary for acquiring vector stray field maps, is applied along the NV axis. From the images, it is evident that the bias field does not significantly affect the NV-PL contrast. ODMR spectra acquired at the locations marked in Figure S7(a) indicate that, along the FM stripe, there is no significant magnetic field component perpendicular to the NV axis that could lead to spin mixing. Instead, we are primarily sensing the OOP field components that are aligned with the NV axis, which results in a symmetric Zeeman shift with respect to  $f_0=2.87$  GHz, as can be seen in Figure S7(d).

## **Section 8: Iso-B contours**

The acquisition of NV-PL images under MW excitation at a given frequency allows us to resolve iso-field contours, as can be observed in Figure S8. The images show contours of regions with a given stray field value together with the PL quenching along the FM stripe between AF domains. From the images, we can see the relative position of the different contours with respect to the FM stripe. Negative and positive values of the stray field are resolved by applying a bias field of 25 mT along the NV-axis. Pure iso-B images can be obtained when the NV-PL image acquired without MW excitation is subtracted. The dual iso-B images shown in the main text are obtained by taking the PL difference between two iso-B images.

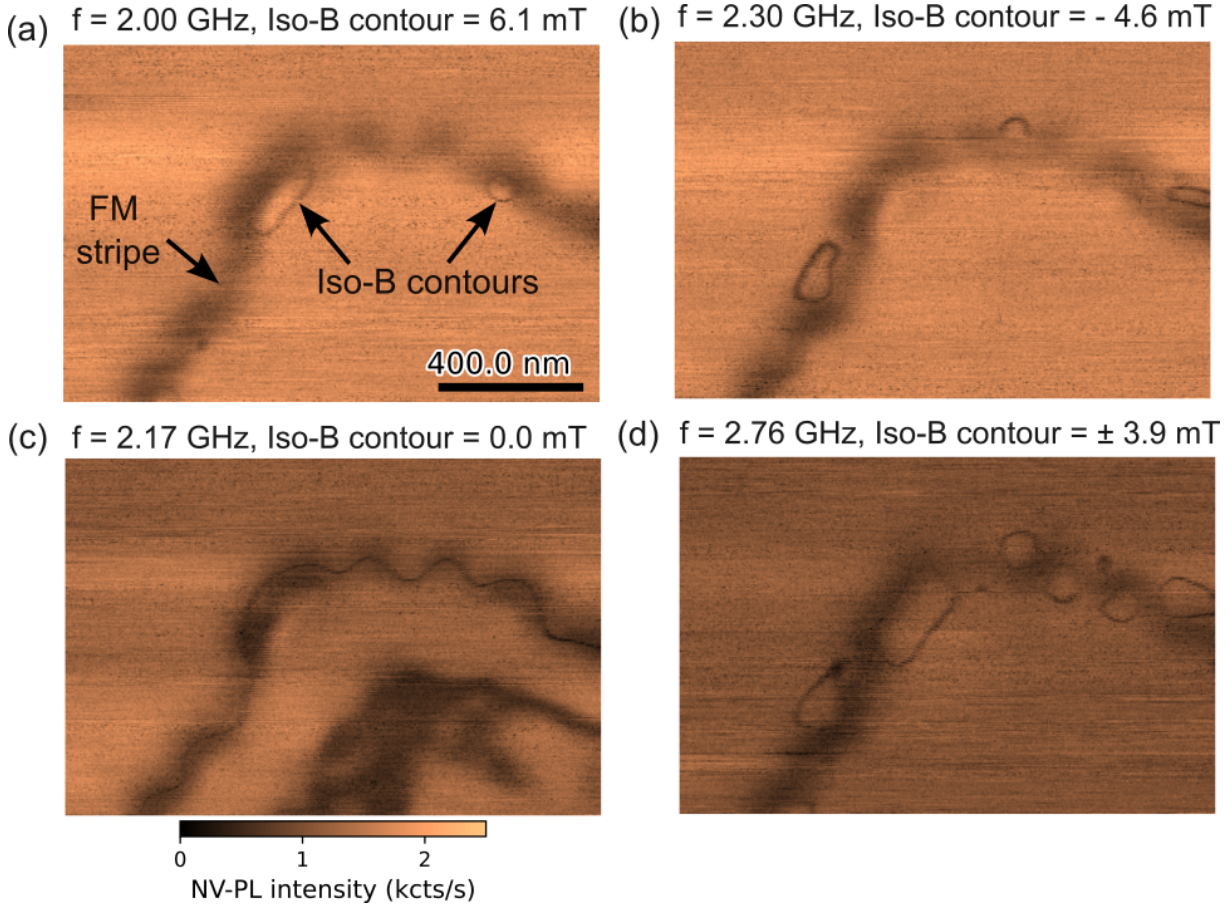


Figure S8: **Iso-B contours and NV-PL maps.** NV-PL images acquired while applying MW excitation to the NV at (a) 2.00 GHz, (b) 2.30 GHz, (c) 2.17 GHz, and (d) 2.76 GHz. A bias field of 25 mT was applied to record the images in (a)-(c), and 0 mT for the image in (d).

## Section 9: Reconstruction of the vector field components

In general, for static magnetic fields in source-free regions, the magnetic field components are not independent. Therefore, it is possible to derive all three field components above the sample surface at a given distance from the measurement of any single component.<sup>3,4</sup> By using Ampere's law and applying the reverse propagation method in Fourier space, we can obtain the field components ( $B_x, B_y, B_z$ ), at a constant  $d_{\text{NV}}$  using the measured  $B_{\text{NV}}$  projection, as given by:

$$B_x(k_x, k_y, d_{\text{NV}}) = -i \frac{k_x}{k} B_z(k_x, k_y, d_{\text{NV}}), \quad B_y(k_x, k_y, d_{\text{NV}}) = -i \frac{k_y}{k} B_z(k_x, k_y, d_{\text{NV}}), \quad (5)$$

with,

$$B_z(k_x, k_y, d_{\text{NV}}) = \frac{B_{\text{NV}}(k_x, k_y, d_{\text{NV}})}{n_z - i \frac{n_x k_x + n_y k_y}{k}}. \quad (6)$$

with  $\hat{e}_{\text{NV}} = \cos \varphi_{\text{NV}} \sin \theta_{\text{NV}} \hat{e}_x + \sin \varphi_{\text{NV}} \sin \theta_{\text{NV}} \hat{e}_y + \cos \theta_{\text{NV}} \hat{e}_z = n_x \hat{e}_x + n_y \hat{e}_y + n_z \hat{e}_z$  and  $k = \sqrt{k_x^2 + k_y^2}$ .  $\mathbf{k} = (k_x, k_y)$  is the wave-vector.

In section 2 we obtained  $\varphi_{\text{NV}} = 0^\circ$  and  $\theta_{\text{NV}} = 180^\circ$ . Therefore,  $n_x = n_y = 0$  and  $n_z = -1$ , and from the equation (6),  $B_z(k_x, k_y, d_{\text{NV}}) = -B_{\text{NV}}(k_x, k_y, d_{\text{NV}})$ . The IP stray field maps shown in Figure 4 of the main text were reconstructed after applying the inverse Fourier transform to the values obtained using the expressions in (5).

## section 10: Close-up view of the ODMR contrast on AF domains

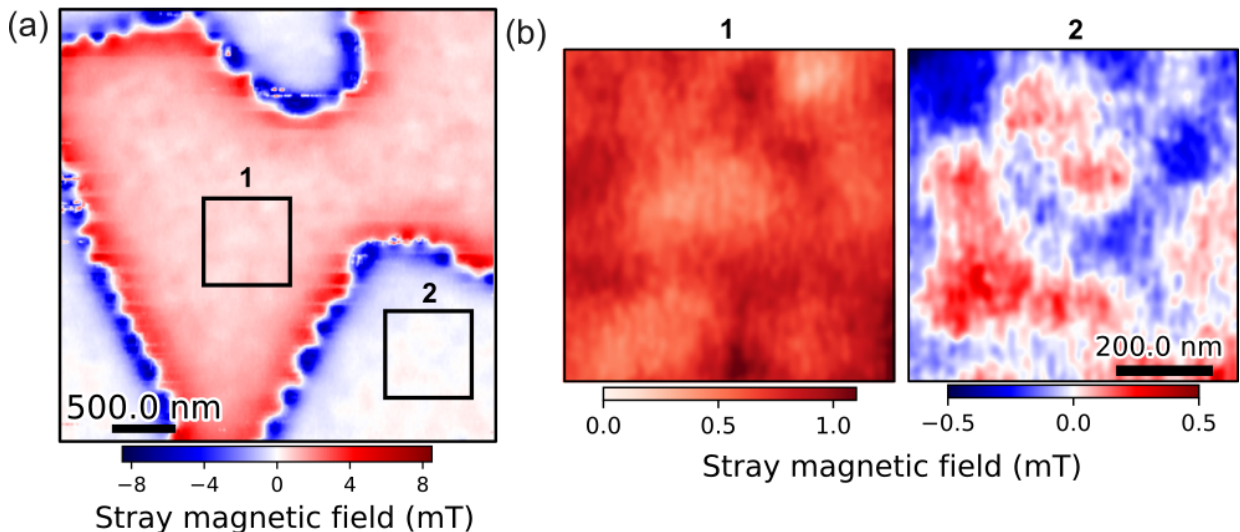


Figure S9: **ODMR contrast in the ROI.** (a) ODMR map shown in Figure 4(a) of the main text. (b) Close-up view in the ROI 1 and 2.

As described in the main text, a stray magnetic field of hundreds of  $\mu\text{T}$  up to around 1 mT is measured on the AF domains. In Figure S9, the close-up view of the region of interest (ROI) 1 and 2 in the ODMR map in Figure 4(a) in the main text show inhomogeneities of the stray field and thus imply the formation of small magnetization variations inside the AF domains. The observed variation of the stray field in the AF domains is most likely produced by uncompensated magnetization induced by local variation of the thin film thicknesses or due to granularity in the morphology of the sample surface. The morphology and granularity of the sample surface can be observed in the topography AFM images in Figure S10(a) and S10(b), acquired simultaneously with the MFM image shown in Figure S10(c).

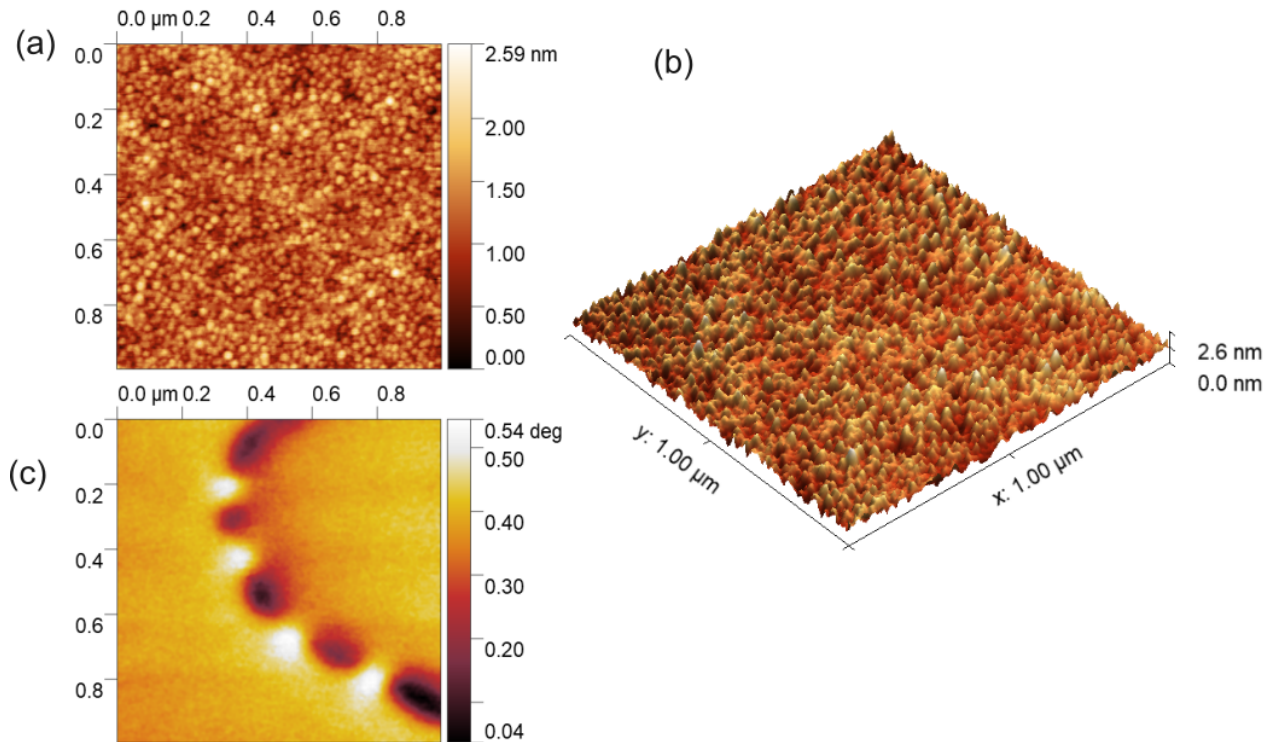


Figure S10: **Topography and MFM images.** (a)  $1\mu\text{m} \times 1\mu\text{m}$  2D and (b) 3D AFM topography image. (c)  $1\mu\text{m} \times 1\mu\text{m}$  MFM images.

## Section 11: OOP magnetization and DW shift

Figure S11(a) shows a 3D representation of the simulated structure with a square AF domain and sharp DW. The structure is modeled as four FM blocks with magnetization up and

down for AF coupling. The OOP magnetization of the FM blocks 1 and 3 is the same, and it is shown in the top image of Figure S11(b). The bottom image corresponds to the magnetization of blocks 2 and 4. To visualize the DW shift between the adjacent FM blocks, an overlap of the magnetization is shown in Figure S11(c). The DW shift at the position indicated by the white arrows in the top image in Figure S11(c) can be estimated by plotting the profile across the DW in the first and second FM block. The profiles are depicted in Figure S11(d), obtaining a lateral shift  $\delta \approx 40$  nm between DWs. This lateral shift is not uniform along the boundary of the AF domains, in some regions  $\delta$  can goes down to 0 nm.

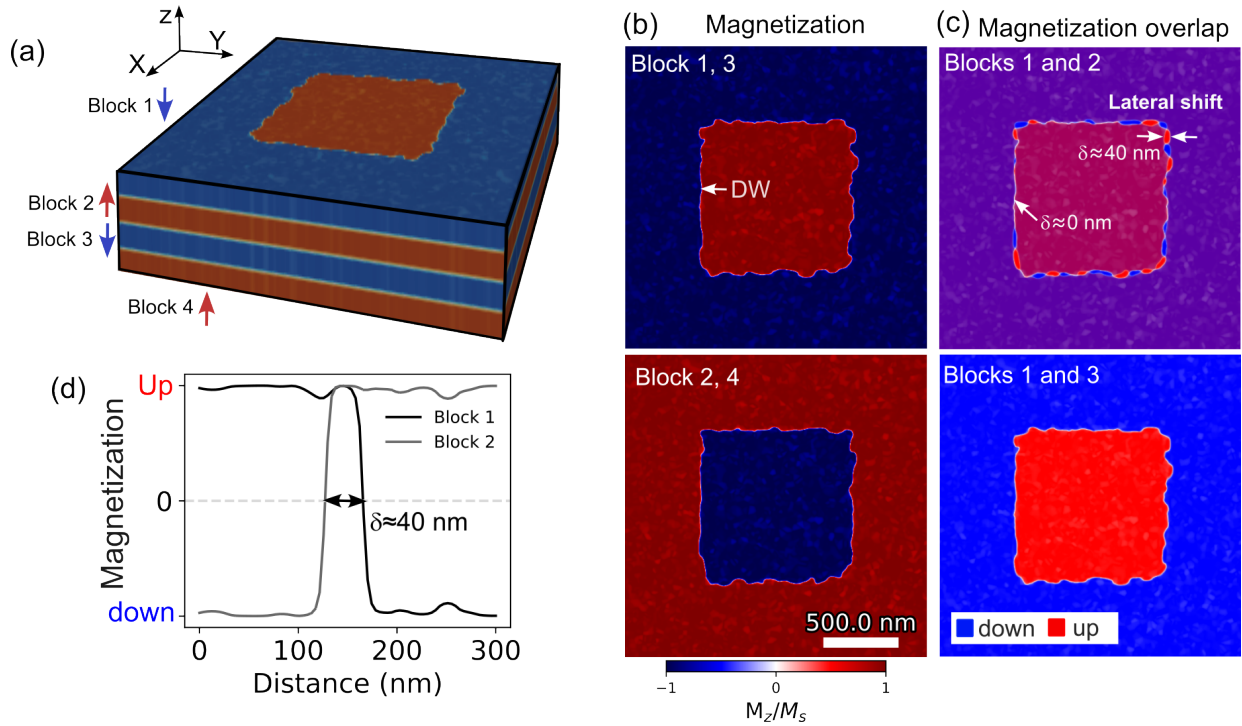


Figure S11: **DW-shift.** (a) Three-dimensional structure of the simulated square AF domain with sharp DW. (b) Top (bottom) image correspond to the OOP magnetization of the FM Blocks 1 and 3 (2 and 4). (c) OOP magnetization overlap of two different FM blocks to visualize the DW shift  $\delta$ . (d) Magnetization profile and DW shift between the FM blocks block 1 and 2 (3).

### Code for simulation of magnetization

```
***** Interaction Energy Parameters *****/
A := 8.0e-12 //Heisenberg exchange [J/m]
```

```

Aex = A

A_IEC := -0.7e-3 // Interlayer exchange [J/m^2]

Ku1 = 0.6e6 // Uniaxial anisotropy downward [J/m^3]

anisU = vector(0, 0, 1) // Direction of anisotropy axis

alpha = 0.01 // Gilbert damping

***** Number of layers, GridSize, CellSize and geometry *****/
Lx := 2048e-9

Ly := 2048e-9

cyldiam := 1024e-9

dz := 0.75e-9 // Corresponds to the Ru layer

ithickness := 6.75e-9

N := 4 // Number of Co/Pt blocks (N-1 is the number of Ru layers)

X := 9 // Number of layers of thickness dz in a Co/Pt block

Nx := 512

Ny := 512

Nz := N*X + N - 1

Lz := Nz * dz

print("Nz=", Nz)

//Nz= 39

SetGridsize(Nx, Ny, Nz)

SetCellsize(Lx/Nx, Ly/Ny, dz)

SetPBC(8, 8, 0)

***** Magnetic parameters of the sample *****/
Ms := 833e3 //Saturation magnetization [A/m]

Msat = Ms

ALL_layers := Layers(0, nz)

FM_layers := Layers(0, X)

for i := 1; i < N; i++ {

    FM_layers = FM_layers.add(Layers(i*(X+1), (i+1)*(X+1)-1))
}

```

```

}

setGeom(FM_layers)

IEC_layers_up := Layer(X + 1)

for i := 1; i < N-1; i++ {

  IEC_layers_up = IEC_layers_up.add(Layer(X + 1 + i*(X+1)))

}

IEC_layers_dn := Layer(X - 1)

for i := 1; i < N-1; i++ {

  IEC_layers_dn = IEC_layers_dn.add(Layer(X - 1 + i*(X+1)))

}

pf := Const((A_IEC) / (dz * Ms))

up := Masked(Shifted(m, 0, 0, 2), IEC_layers_up)

dn := Masked(Shifted(m, 0, 0, -2), IEC_layers_dn)

Bc := Mul(pf, Add(up, dn))

AddFieldTerm(Bc)

AddEdensTerm(Mul(Const(-0.5), Dot(Bc, M_full)))

r0 := cuboid(cyldiam, cyldiam, X*dz).transl(0, 0, -Lz/2+X*dz/2)

a0 := cuboid(Lx, Ly, X*dz).transl(0, 0, -Lz/2+X*dz/2).sub(r0)

r1 := r0.transl(0, 0, (X+1)*dz)

a1 := a0.transl(0, 0, (X+1)*dz)

r2 := r1.transl(0, 0, (X+1)*dz)

a2 := a1.transl(0, 0, (X+1)*dz)

r3 := r2.transl(0, 0, (X+1)*dz)

a3 := a2.transl(0, 0, (X+1)*dz)

m.SetInShape(a0, Uniform(0, 0, 1))

m.SetInShape(r1, Uniform(0, 0, 1))

m.SetInShape(a2, Uniform(0, 0, 1))

m.SetInShape(r3, Uniform(0, 0, 1))

```

```

m.SetInShape(r0, Uniform(0, 0, -1))
m.SetInShape(a1, Uniform(0, 0, -1))
m.SetInShape(r2, Uniform(0, 0, -1))
m.SetInShape(a3, Uniform(0, 0, -1))

grainSize := 32e-9

randomSeed := 7913279

maxRegion := 256

ext_makegrains(grainSize, maxRegion, randomSeed)

randSeed(randomSeed)

theta_max := 20.0

for i := 0; i < maxRegion; i++ {

    theta := theta_max / 3 * randNorm()

    theta = theta / 180 * pi

    phi := PI * rand()

    vu := vector(sin(theta)*cos(phi), sin(theta)*sin(phi), cos(theta))

    anisU.SetRegion(i, vu)

}

B := 0.001 // slight 1 mT offset field to facilitate the relaxation and minimization

Theta := 0.5

Theta = Theta / 180 * pi

Phi := 0.5

Phi = Phi / 180 * pi

MinimizerStop = 1e-6

TableAddVar(m.Average().Dot(vector(sin(Theta)*cos(Phi), sin(Theta)*sin(Phi), cos(Theta))), "<M>", "none")

TableAdd(Edens_total)

B_ext = vector(B*sin(Theta)*cos(Phi), B*sin(Theta)*sin(Phi), B*cos(Theta))

TableAdd(B_ext)

TableAddVar(B, "Bext", "T")

```

```

relax()

saveas(m, "relaxed.ovf")

minimize()

saveas(m, "minimized.ovf") // this relaxed and subsequently minimized state is the one we use

```

### Code for simulation of stray field maps

To simulate the stray field from the magnetic state obtained from the previous code, we defined a larger simulation domain (larger Nz), loaded the magnetic state with the m.loadfile command, and fitted it into the simulation domain with the m.getcell and m.setcell commands. Finally, the field is calculated

```

A := 8.0e-12

Aex = A

A_IEC := -0.7e-3

Ku1 = 0.6e6

anisU = vector(0, 0, 1)

alpha = 0.01

Lx := 2048e-9

Ly := 2048e-9

cyldiam := 1024e-9

dz := 0.75e-9

ithickness := 6.75e-9

N := 4

X := 9

Nx := 512

Ny := 512

Nz := N*X + N - 1 + 100

nzlayers := N*X + N - 1

totalt := Nz * dz

```

```

thickness := 100 * dz

Lz := Nz * dz

print("Nz=", Nz)

//Nz= 139

SetGridsize(Nx, Ny, Nz)

SetCellsize(Lx/Nx, Ly/Ny, dz)

SetPBC(8, 8, 0)

//resizing...

Ms := 833e3

Msat = Ms

m.loadfile("N4X6-strayfield.out/minimized.ovf")

for i := 0; i < Nx; i += 1 {

  for j := 0; j < Ny; j += 1 {

    a := m.getcell(i, j, 0)

    b := m.getcell(i, j, 45)

    c := m.getcell(i, j, 90)

    d := m.getcell(i, j, 135)

    m.setcell(i, j, 0, a)

    m.setcell(i, j, 1, a)

    m.setcell(i, j, 2, a)

    m.setcell(i, j, 3, a)

    m.setcell(i, j, 4, a)

    m.setcell(i, j, 5, a)

    m.setcell(i, j, 6, a)

    m.setcell(i, j, 7, a)

    m.setcell(i, j, 8, a)

    m.setcell(i, j, 10, b)

    m.setcell(i, j, 11, b)

    m.setcell(i, j, 12, b)
  }
}

```

```

m.setcell(i, j, 13, b)
m.setcell(i, j, 14, b)
m.setcell(i, j, 15, b)
m.setcell(i, j, 16, b)
m.setcell(i, j, 17, b)
m.setcell(i, j, 18, b)
m.setcell(i, j, 20, c)
m.setcell(i, j, 21, c)
m.setcell(i, j, 22, c)
m.setcell(i, j, 23, c)
m.setcell(i, j, 24, c)
m.setcell(i, j, 25, c)
m.setcell(i, j, 26, c)
m.setcell(i, j, 27, c)
m.setcell(i, j, 28, c)
m.setcell(i, j, 30, d)
m.setcell(i, j, 31, d)
m.setcell(i, j, 32, d)
m.setcell(i, j, 33, d)
m.setcell(i, j, 34, d)
m.setcell(i, j, 35, d)
m.setcell(i, j, 36, d)
m.setcell(i, j, 37, d)
m.setcell(i, j, 38, d)
}

}

ALL_layers := Layers(0, nzlayers)
FM_layers := Layers(0, X)
for i := 1; i < N; i++ {

```

```

FM_layers = FM_layers.add(Layers(i*(X+1), (i+1)*(X+1)-1))

}

setGeom(FM_layers)

saveas(B_demag, "B_demag_all")

```

## **Section 12: $T_1$ measurement with different NV-probes**

Figure S12 show local  $T_1$  measurements performed with different scanning diamond probes and represented in Figure 5 in the main text.

## **Section 13: NV-PL quenching contrast and laser power**

The quenching observed in the NV-PL maps acquired with the (111)-NV probe is produced by magnetic noise. The perpendicular components of the noise that are resonant with the NV transition affect  $T_1$  and reduce the PL intensity, as can be seen in Figure S12. There is a competition between the optical pumping from the excitation power of the green laser and the spin relaxation.<sup>5</sup> That means that the contrast in the NV-PL maps should be affected by the excitation power. Figure S13 shows a saturation curve measured on the (111)-NV tip with the sample engaged, from which we obtain a saturation power of  $85 \mu\text{W}$ . Additionally, NV-PL maps acquired in the same region with different excitation power are depicted in the figure. We can observe that there is not a significant change in the contrast of the NV-PL maps. This could be due to the fact that, in contrast to what has been observed in AF samples,<sup>5</sup> the field produced on the FM cores around the DWs could affect the competition between the optical pumping and the spin relaxation process.

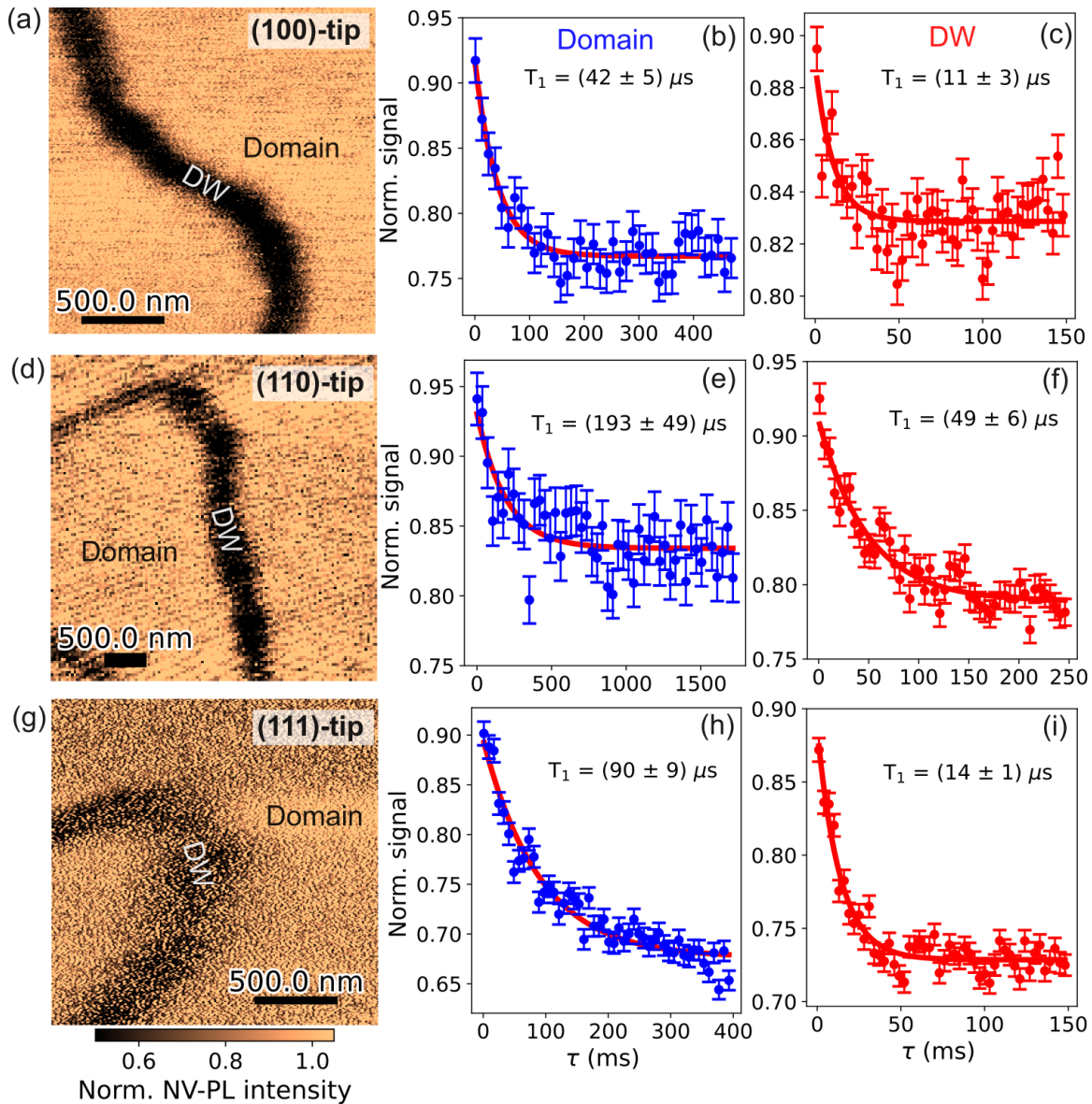


Figure S12: **Local  $T_1$  measurements.** NV-PL quenching map, and  $T_1$  measurement on a domain and a DW, acquired with (a)-(c) a (100)-NV tip, (d)-(f) a (110)-NV tip, and (g)-(i) a (111)-NV tip.

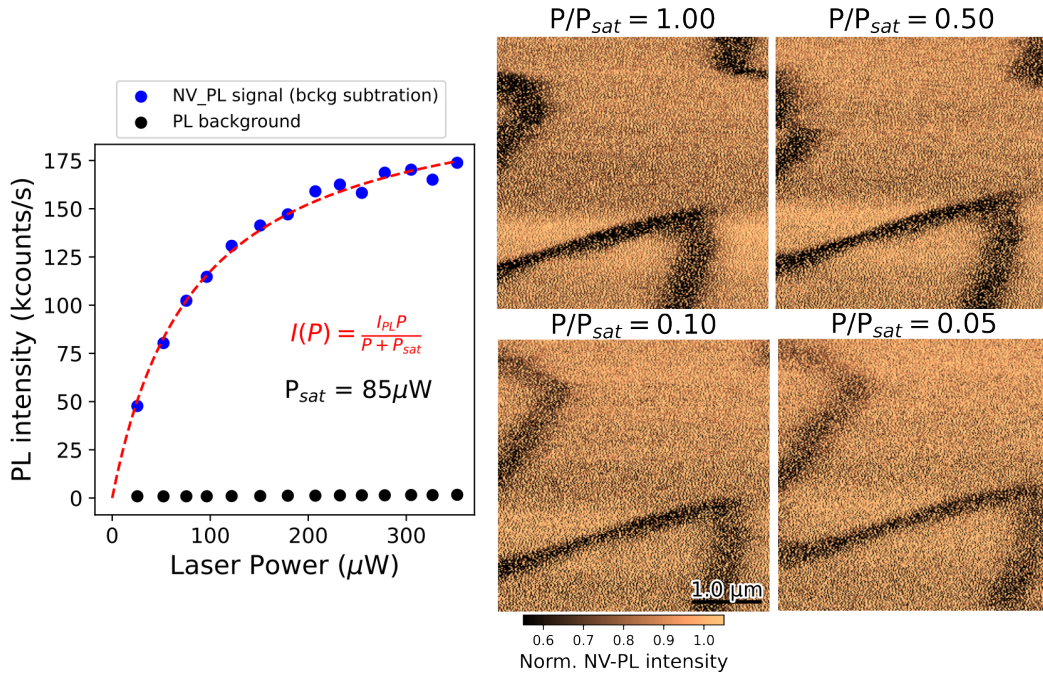


Figure S13: **NV-PL quenching contrast vs laser power.** Saturation curve measured on the (111)-diamond probe and NV-PL quenching images recorder with different excitation power below saturation.

## References

- (1) Hingant, T.; Tetienne, J.-P.; Martínez, L. J.; Garcia, K.; Ravelosona, D.; Roch, J.-F.; Jacques, V. Measuring the Magnetic Moment Density in Patterned Ultrathin Ferromagnets with Submicrometer Resolution. *Phys. Rev. Appl.* **2015**, *4*, 014003.
- (2) Hellwig, O.; Berger, A.; Fullerton, E. E. Domain Walls in Antiferromagnetically Coupled Multilayer Films. *Phys. Rev. Lett.* **2003**, *91*, 197203.
- (3) Lima, E. A.; Weiss, B. P. Obtaining vector magnetic field maps from single-component measurements of geological samples. *Journal of Geophysical Research: Solid Earth* **2009**, *114*.
- (4) Dovzhenko, Y.; Casola, F.; Schlotter, S.; Zhou, T. X.; Büttner, F.; Walsworth, R. L.; Beach, G. S.; Yacoby, A. Magnetostatic twists in room-temperature skyrmions explored

by nitrogen-vacancy center spin texture reconstruction. *Nature communications* **2018**, *9*, 2712.

(5) Finco, A. et al. Imaging non-collinear antiferromagnetic textures via single spin relaxometry. *Nat. Commun.* **2021**, *12*, 767.